NASA Technical Paper 1770

Radio-Wave Propagation for Space Communications Systems

Louis J. Ippolito

FEBRUARY 1981

NASA

NASA Technical Paper 1770

Radio-Wave Propagation for Space Communications Systems

Louis J. Ippolito
NASA Office of Space and Terrestrial Applications
Washington, D.C.

National Aeronautics
and Space Administration

**Scientific and Technical
Information Branch**

1981

CONTENTS

CHAPTER 1

INTRODUCTION

Radio-wave propagation plays an important part in the design and performance of space communications systems. The degrading effect of precipitation in the transmission path is a major concern associated with space communications systems, particularly for those operating above 10 GHz. At these frequencies, absorption and scattering caused by rain, hail, ice crystals, or wet snow can cause a reduction in transmitted signal amplitude (attenuation) that lowers the reliability and performance of the space communications link. Other effects can be generated by precipitation on the Earth/space path. They include depolarization, rapid amplitude and phase fluctuations (scintillations), antenna gain degradation, and bandwidth coherence reduction.

Even apparent "clear sky" conditions can produce propagation effects that can degrade or change the transmitted radio wave. Constituent gases in Earth's atmosphere, particularly oxygen and water vapor, interact with the radio wave and reduce the signal amplitude by an absorption process. Turbulence or rapid temperature variations in the transmission path can cause amplitude and phase scintillations or depolarize the wave. Clouds, fog, dirt, sand, and even severe air pollution can cause observable propagation effects. Finally, background sky noise is always present and contributes directly to the noise performance of the communications receiver system.

The relative importance of the various radio-wave propagation factors depends to a large extent on the frequency of operation of the Earth/space link, as well as on the local climatology, local geography, type of transmission, and elevation angle to the satellite. Generally, the effects become more significant as the frequency increases and as the elevation angle decreases; however, there are exceptions, as will be described later in this review paper. The randomness and general unpredictability of the phenomena that produce the propagation variations add a further dimension of complexity and uncertainty to the evaluation of radio-wave propagation in space communications. Statistical approaches have been found to be the most useful in evaluation of many of the problem areas.

Before beginning the discussion of propagation effects, a brief review of the historical development of space communications will be helpful in pointing out some of the trends and developments that have had a direct bearing on the types of propagation phenomena that are important in space communications.

Evolution of Satellite Communications

The growth in the number of orbiting satellites launched for space science and applications over the past two decades has been phenomenal. Prior to 1970, only a handful of communications satellites

were in active geosynchronous orbit. These included seven INTELSAT international satellites operating in the 4- to 6-GHz frequency bands; NASA experimental satellites SYNCOM 3, ATS 1, ATS 3, and ATS 5, the first of the United Kingdom's SKYNET satellites, and the first TACSAT of the U.S. Air Force (refs. 1 and 2). The interval 1970–74 saw more than two dozen additional geosynchronous satellites placed into orbit, including the first communications satellites of Canada and the U.S.S.R. The period 1975–79 produced over seventy new satellites in orbit, including several that introduced new services in the meteorological, mobile, and direct broadcast areas. Japan, Indonesia, and Europe (European Space Agency) also joined the list of satellite-producing countries, while the U.S. domestic communication satellite fleet expanded with systems developed by COMSAT General, RCA Americom, and Western Union Telegraph Co. The decade of the 1980s promises to bring an explosion of new satellites, services, and capabilities into space, with over 70 new satellites planned for launch in the next 5 years. Eight additional countries are expected to join the list of satellite-producing organizations by 1985. The emergence of second-generation satellites and regional systems has further accelerated the growth of satellite applications.

The Frequency Spectrum and Sharing

There are three major factors in the development of satellite communication that have increased the need for further awareness and understanding of the radio-wave propagation variables involved. The first of these factors, the rapid increase in the use of the frequencies below 6 GHz allocated for satellite services, has produced conditions of spectrum crowding and sharing that have required the systems designer to look to the higher frequency bands to relieve the congestion. The bands allocated for fixed satellite service in the 12/14 and 20/30 GHz bands and for broadcast satellite service in the 11.7- to 12.2-GHz band are already being used on present experimental satellites and are planned for operational systems over the next several years. Allocations for many other space services, including space research, Earth exploration, meteorology, mobile communication, and radio navigation, are available from 10 GHz to well over 100 GHz. Most of these allocations are exclusive, that is, they are not shared with other space or terrestrial services, and this makes them attractive due to the lack of potential sharing and coordination problems that are present in the bands below 10 GHz. The trend to higher and higher operational frequencies can be seen in figure 1, which shows the number of geosynchronous satellites in each of a series of increasing frequency bands launched in orbit or planned for 5-year intervals from 1965 through the mid 1980s. The greatest expansion is seen in the 11- to 17-GHz region, in which several operational satellites in the 12- to 14-GHz fixed satellite service band are planned. The region above 20 GHz remains primarily for experimental satellites in the 20/30 GHz bands and for propagation beacons extending to 34.8 GHz.

Communications Traffic Growth

A second major factor in satellite communications that has tended to push the development of satellite systems to higher operating frequencies has been the expanded need for more bandwidth to accommodate the exploding information transfer requirements of our technological society. Present fixed satellite service allocations in the 4/6 and 7/8 GHz bands, which support virtually all domestic, international, and military communications presently in operation, total 500 MHz in each

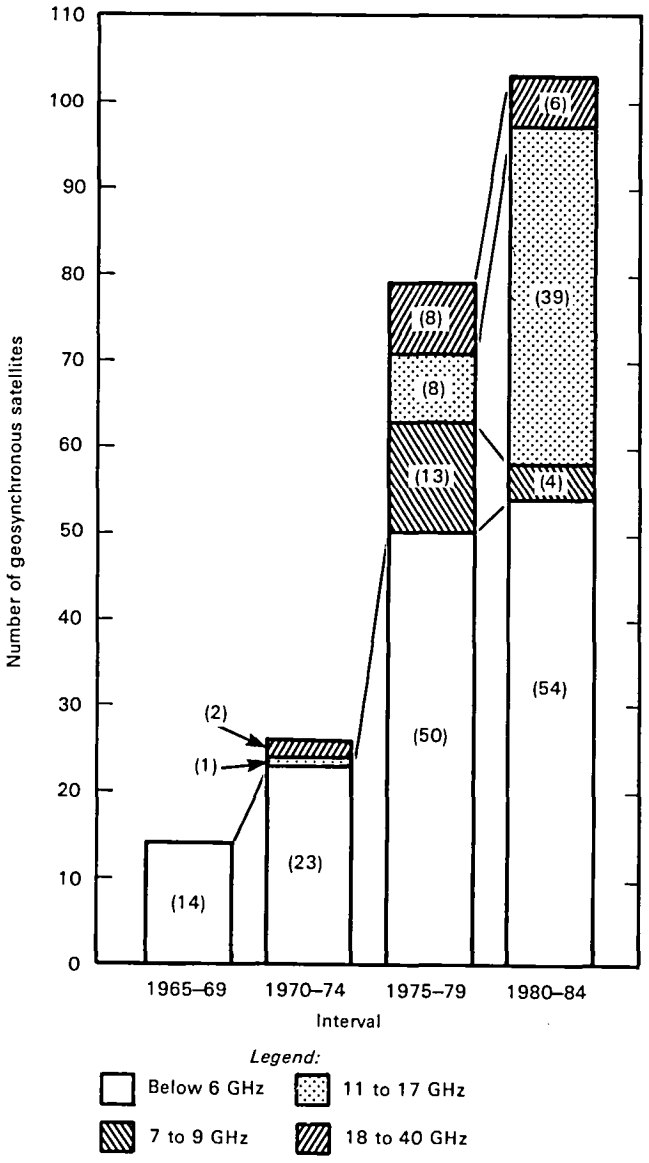

Figure 1.—Use of frequency bands in the development of geosynchronous satellites (already placed into orbit or planned) from 1965 through 1984.

band. Above 10 GHz, however, the available bandwidth expands dramatically. Present allocations developed at the 1979 World Administrative Radio Conference provide for bandwidths of over 500 MHz in the 12/14 GHz region, 3.5 GHz in the 20/30 GHz region, and 3 GHz in the 40- to 43-GHz region. The total bandwidth presently allocated to fixed satellite service in the bands above 10 GHz is over 40 GHz, extending to the upper limit of allocations at 275 GHz.

The decade of the 1970s began with a surplus of available communications capacity on North American domestic satellites (Domsats), but in the 1980s we are already faced with a shortage of available transponder capacity. Current U.S. Domsats, all operating in the 4/6 GHz band, number about 156 total transponders. Present filings with the Federal Communications Commission, however, provide a potential for 19 new satellites in orbit by 1985, with over 500 transponders in both the 4/6 and 12/14 GHz bands.

Orbit Congestion

The third major factor in the movement to higher operating frequencies concerns the limited number of orbital positions or "slots" available in the geostationary orbit for space communications. For example, the segment of the geostationary arc permitting the use of ground station elevation angles above 5° for the contiguous 48 States in the United States is from 60° to 140° W. Assuming a nominal spacing between fixed service communications satellites of 4°, which is typical for satellites operating in the 4/6 GHz band, 20 slots are available. For a spacing of 3°, which is typical for satellites operating at 12/14 GHz, the total is 27 slots. If coverage is to be provided to all 50 States, the usable segment reduces to 100° to 140°, and the numbers of slots in each of the two bands become 10 and 13, respectively. At the present time, domestic United States and Canadian organizations have 12 slots at 4/6 GHz and 10 slots at 12/14 GHz occupied or committed. Thus, even in the absence of other Western Hemisphere nations employing space systems, and disregarding the shared 12/14 GHz allocation with broadcasting service satellites, which would require wider spacing, the American arc will be essentially filled at 4/6 GHz frequencies and over 50 percent of capacity at 12/14 GHz frequencies within 3 to 5 years. A number of techniques have been proposed or are under active development for more efficient utilization of the orbital arc. These techniques include frequency reuse employing polarization and spatial diversity, spot beams for increased link reliability during adverse weather conditions, multiple beam satellite antennas switched or scanned to cover large service areas, and larger aperture narrow beamwidth systems to reduce intersatellite interference. All of these techniques, particularly those requiring larger aperture antennas and multiple beam switching, can be most efficiently accomplished at the higher frequencies, where component size and weight are more compatible with spaceborne constraints.

In the next chapter the fundamental radio-wave propagation factors of importance to space communications systems (operating in the bands above 1 GHz) are discussed.

CHAPTER 2

FUNDAMENTALS OF RADIO-WAVE PROPAGATION

Transmission Principles

An electromagnetic wave, referred to as a radio-wave at radio frequencies, is characterized by variations of electric and magnetic fields. The oscillating motion of the field variations vibrating at a particular point in space at a frequency f, excites similar vibrations at neighboring points, and the radio wave is said to travel or to "propagate." The wavelength λ of the radio wave is the spatial separation of two successive oscillations, which is the distance the wave travels during one cycle of oscillation. The frequency and wavelength in free space are related by the equation $\lambda = c/f$, where c is the phase velocity of light.

The power density, in watts per square meter, of a radio wave propagating from a source is inversely proportional to the square of the distance to the source. From this result, often called the inverse square law of radiation, a free space attenuation, or transmission loss, usually expressed in decibels, between two points in a radio-wave link may be calculated as

$$L_a = 20 \log \frac{4\pi d}{\lambda} \tag{1}$$

where

L_a = free space attenuation (a positive value), in dB
d = distance between the transmitting and receiving points
λ = wavelength

and d and λ are expressed in the same unit of length.

Free space attenuation is present for all radio waves propagating in free space or in regions where the uniformity of free space is approximated, such as Earth's atmosphere.

The frequency of the radio wave is a critical factor in determining whether other impairments to space communications in addition to the free space attenuation determined by the separation distance between transmitter and receiver will be introduced by Earth's atmosphere. The radio wave will propagate from Earth's surface to outer space provided its frequency is high enough to penetrate the ionosphere, which is the ionized region extending from about 50 km to roughly 2000 km above the surface. The various regions (or layers) in the ionosphere, designated D, E, and F, respectively, in order

of increasing altitude, act as reflectors or absorbers to radio waves at frequencies below about 10 to 20 MHz, and space communications are not practical. As the frequency is increased, the reflection properties of the E and F layers are reduced and the signal will propagate through. Radio waves above 30 MHz will propagate through the ionosphere; however, the properties of the wave could be modified or degraded to varying degrees depending on frequency, geographic location, and time of day. Ionospheric effects tend to become less significant as the frequency of the wave increases, and above about 3 GHz the ionosphere is essentially transparent to space communications, with some notable exceptions, which will be discussed later.

Space communications above the ionospheric penetration frequency of about 30 MHz will proceed unimpeded as the frequency of transmission is increased up to frequencies at which point the gaseous constituents of the lower atmosphere, or troposphere, primarily oxygen and water vapor, will absorb energy from the radio wave. At certain specific "absorption bands," where the radio wave and gaseous interaction are particularly intense, space communications are severely limited. It is in the "atmospheric windows" between absorption bands that practical Earth/space communications have developed, and it is in those windows that we focus our attention in the evaluation of radio-wave propagation factors.

The major radio wave propagation factors that are significant in space communications operating in the atmospheric windows up to about 100 GHz are as follows:

(1) Absorption attenuation caused by atmospheric gases
(2) Scattering and absorption attenuation caused by hydrometeors (such as rain, hail, wet snow, and clouds)
(3) Depolarization caused by hydrometeors, multipath propagation, and Faraday rotation
(4) Noise emission caused by gaseous absorption and hydrometeors
(5) Scintillation (rapid variations) of amplitude and phase caused by turbulence or refractive index irregularities
(6) Angle of arrival variations caused by small-scale fluctuations in refractive index
(7) Bandwidth limitations caused by the multipath and dispersive properties of the atmosphere
(8) Antenna gain degradations caused by phase decorrelation across aperture

The fundamental characteristics of each factor will be discussed in the remainder of this review paper.

Gaseous Absorption

There are many gaseous constituents of Earth's atmosphere that can interact with electromagnetic waves; however, at radio-wave frequencies only oxygen and water vapor will produce significant absorption. The first three absorption bands are centered at frequencies of 22.2 GHz (H_2O), 60 GHz (O_2), and 118.8 GHz (O_2). The permanent magnetic moment of the oxygen molecule interacts with the magnetic field of the radio wave and the water vapor molecule electric dipole interacts with the electric field of the wave producing a quantum level change in the rotational energy of the molecule, which absorbs energy from the radio wave. The frequency dependence of the absorption has been found to depend on an empirical line width constant that is a function of temperature, pressure, and the humidity

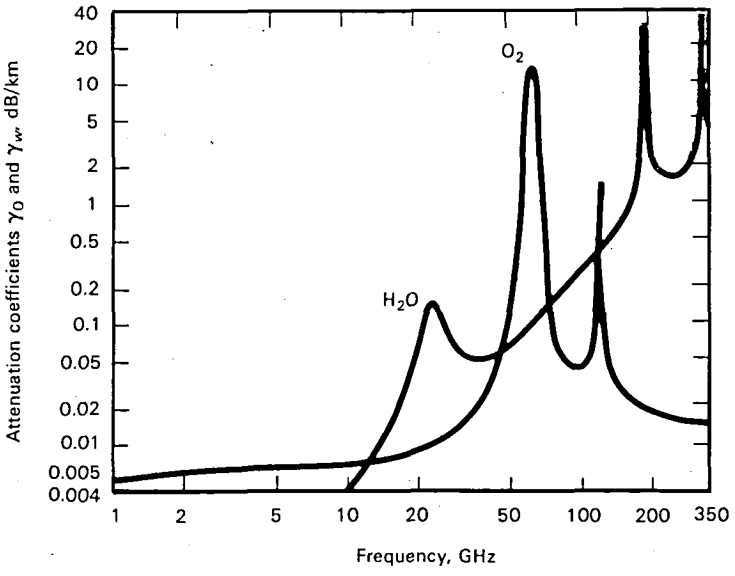

Figure 2.—Attenuation coefficients for oxygen and water vapor from 1 to 350 GHz. (Pressure = 1 atm (1.013×10^5 P); temperature: 20° C; water vapor density: 7.5 g/m^3.)

of the atmosphere (ref. 3). All of these parameters are highly variable with altitude, location, and time of day.

The total gaseous attenuation A in the atmosphere over a path length r_0 (in kilometers) is given by

$$A_a = \int_0^{r_0} [\gamma_O(r) + \gamma_w(r)]\, dr \qquad \text{dB} \qquad (2)$$

where γ_O and γ_w are the attenuation coefficients (in decibels per kilometer) for oxygen and water vapor, respectively. Figure 2 shows the attenuation coefficients for oxygen and water vapor for frequencies from 1 to 350 GHz at a temperature of 20° C, and a humidity of 7.6 g/m^3 (ref. 4).

Figure 3 shows the estimated one-way zenith attenuation for frequencies between 1 and 300 GHz calculated for vertical ray paths through a spherically stratified atmosphere (ref. 4). Curve A shows the

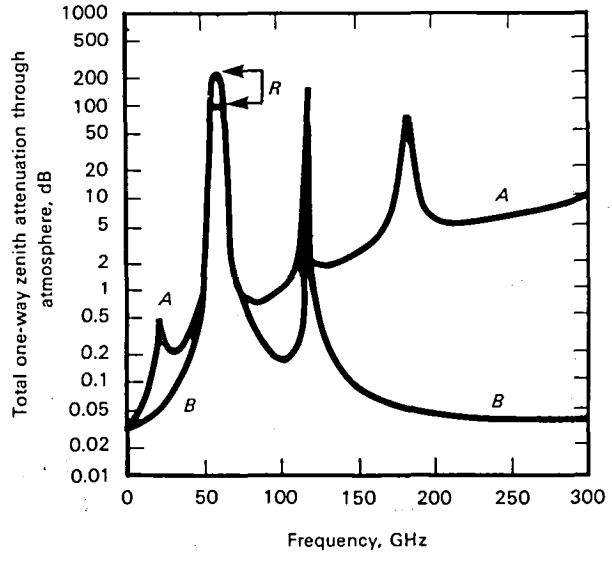

Figure 3.—Total one-way zenith attenuation through the atmosphere as a function of frequency. Curve *A:* moderate humidity (7.5 g/m^3 at surface); curve *B:* dry atmosphere (0 g/m^3); region *R:* range of values due to fine structure.

TABLE 1.—ONE-WAY GASEOUS ATTENUATION FOR SATELLITE PATHS THROUGH THE ATMOSPHERE[a]

Frequency, GHz	Total one-way atmospheric attenuation, dB, for elevation angle specified in degrees					
	90°	60°	45°	15°	6°	0°
2	0.034	0.039	0.047	0.13	0.32	1.7
4	.038	.041	.054	.15	.37	1.9
6	.041	.048	.059	.16	.40	2.2
12	.061	.071	.086	.24	.58	4.0
15	.085	.098	.12	.33	.81	5.8
20	.28	.33	.40	1.1	2.7	15
30	.24	.27	.33	.91	2.2	15
41	.41	.47	.58	1.6	3.9	22
94	1.3	1.5	1.8	5.0	12.4	90

[a]Temperature: 20° C; relative humidity: 42 percent; water vapor density: 7.5 g/m^3.

attenuation for a moderately humid atmosphere (7.5 g/m^3 at the surface), and curve *B* for a dry atmosphere (0 g/m^3). The estimation assumes that no condensed water cloud drops or rain are present on the path. The region labeled *R* shows the range of values of the fine structure for the broad oxygen absorption peak at 60 GHz.

Calculations of gaseous attenuation for the total atmosphere at slant paths have been developed from a regression analysis of global surface temperature and absolute humidity data (ref. 5). The model calculates zenith attenuation from the surface of Earth to an 80-km height as a function of frequency, mean local surface temperature, and mean local surface absolute humidity. For slant paths through the atmosphere, the attenuation is given by the cosecant of the elevation angle, down to about 6° of elevation angle, where the cosecant law breaks down because of Earth curvature and refraction effects. Below 6°, the attenuation is obtained by raytracing the path through the atmosphere starting at the surface height and obtaining the line integral of attenuation along the ray path.

Table 1 gives the total one-way gaseous attenuation at several frequencies of interest for satellite communications from 2 to 94 GHz as a function of ground terminal elevation angle. The values are for moderate-humidity (7.5 g/m^3 surface water vapor density) midlatitude locations, with a mean ground temperature of 20° C. Gaseous attenuation is seen to be well below approximately 0.5 dB for frequencies up through 41 GHz, except for elevation angles below 15°.

CHAPTER 3

HYDROMETEOR ATTENUATION IN SATELLITE COMMUNICATIONS

Hydrometeor is the general term referring to the products of condensed water vapor in the atmosphere observed as rain, hail, ice, fog, cloud, or snow. The presence of hydrometeors in the radio-wave path, particularly rain, can produce major impairments in space communications. Raindrops both absorb (attenuate) and scatter radio-wave energy. Other effects produced by rain include depolarization, rapid amplitude and phase fluctuations, antenna gain degradation, and bandwidth coherence reduction.

In the midlatitude regions of the earth, stratiform rain can extend several hundreds of kilometers horizontally, with vertical heights of 4 to 6 km. Convective rains, often associated with thunderstorm events, are of much smaller horizontal extent, usually only several kilometers, but can extend to much greater vertical heights because of convective upwelling. Rain rates in excess of 100 mm/hr (4 in./hr) are not unusual for severe convective rain; however, their duration seldom exceeds several minutes.

The vertical profile of rain cells tends to be uniform up to an altitude of about 4 km, and then decreases very quickly at altitudes up to 6 to 8 km. Figure 4 shows the resulting median rain rate as a function of altitude for several hundred rain cells observed at Wallops Island, Va., during a summer season. The rain rate values were determined from radar reflectivity measurements obtained by Goldhirsh and Katz at 2.8 GHz (ref. 6). The authors note that the falloff height of about 4 km corresponds to the average 0° isotherm height for the summer period, and the falloff rate above that height ranged from about 2 mm/hr per kilometer for the 4 mm/hr surface rain rate to about 45 mm/hr per kilometer for the 143 mm/hr surface value. Results of this type are useful in relating surface rain rate, which can be easily measured, to a path rain rate, which is required to determine total path attenuation for an Earth/space link operating at a given elevation angle.

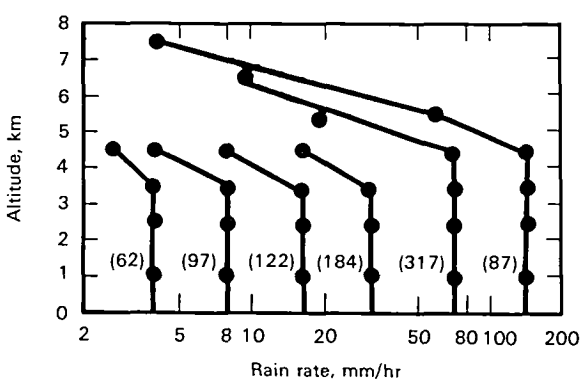

Figure 4.—Mean rain rate profiles for given surface values as measured at Wallops Island, Va., during the summer of 1973. The numbers in parentheses are the number of rain cells measured at that value used to obtain the profiles.

Classical Development for Rain Attenuation

The attenuation of a radio wave propagating in a volume of rain of extent L in the direction of wave propagation can be expressed as

$$A = \int_0^L \alpha \, dx \tag{3}$$

where α is the specific attenuation of the rain volume, expressed in decibels per kilometer. The classical development for the determination of radio-wave attenuation due to rain assumes that the intensity of the wave decays exponentially as it propagates the volume of rain. The waterdrops are usually assumed to be spherical, and the contributions of each drop are additive and independent of the other drops.

The determination of the specific attenuation proceeds from these assumptions. Consider a plane wave of transmitted power P_t incident on a volume of uniformly distributed spherical waterdrops, all of radius a, extending over length L. The received power P_r will be

$$P_r = P_t e^{-kL} \tag{4}$$

where k is the attenuation coefficient for the rain volume (expressed in units of reciprocal length).

The attenuation of the wave, usually expressed as a positive decibel value, is given by

$$A = 10 \log \frac{P_t}{P_r} \tag{5}$$

Converting the log to the base e and employing equation (4),

$$A = 4.343kL \tag{6}$$

The attenuation coefficient k is expressed as

$$k = \rho Q_t \tag{7}$$

where ρ is the drop density (i.e., the number of drops per unit volume) and Q_t is the attenuation cross section of the drop of radius a, expressed in units of area. The value Q_t is the sum of a scattering cross section Q_s and an absorption cross section Q_a. The attenuation cross section is a function of the drop radius r, the wavelength of the radio wave λ, and the complex refractive index of the water drop m:

$$Q_t = Q_t(r, \lambda, m) \tag{8}$$

The drops in a "real" rain are not all of uniform radius, and the attenuation coefficient must be determined by integrating over all drop sizes:

$$k = \int Q_t(r, \lambda, m) n(r) \, dr \tag{9}$$

where $n(r)$ is the drop size distribution. The term $n(r)\,dr$ can be interpreted as the number of drops per unit volume with radii between r and $r + dr$.

The specific attenuation, in decibels per kilometer, may be determined from equations (6) and (9) by letting $L = 1$ km:

$$\alpha = 4.343 \int Q_t(r, \lambda, m)n(r)\,dr \tag{10}$$

Equation (10) emphasizes the dependence of rain attenuation on drop size, drop size distribution, rain rate, and attenuation cross section. The first three parameters are characteristics of the rain structure only; it is through the attenuation cross section that the frequency and temperature dependencies of rain attenuation are observed. All of the parameters in general exhibit time and spatial variabilities that are not deterministic or directly predictable, hence most analyses of rain attenuation must resort to statistical means to quantitatively evaluate the impact of rain on communications systems.

The solution of equation (10) requires Q_t and $n(r)$ as a function of drop size. The value of Q_t is found by employing the classical scattering theory of Mie for a plane wave radiating an absorbing sphere. The resulting series expansion solution for Q_t is found as

$$Q_t = \frac{\lambda^2}{2\pi} \sum_{n=1}^{\infty} (2n + 1)\mathrm{Re}(a_n + b_n) \tag{11}$$

where a_n and b_n are the Mie scattering coefficients, which are complex functions of m, r, and λ (ref. 7).

Several investigators have studied the distributions of raindrop sizes as a function of rain rate and type of storm activity, and the drop size distributions have been found to be well represented by an exponential of the form

$$\begin{aligned} n(r) &= N_0 e^{-\Lambda r} \\ &= N_0 e^{-(cR^{-d})r} \qquad \mathrm{m^{-3}\ mm^{-1}} \end{aligned} \tag{12}$$

where R is the rain rate (in millimeters per hour); r is the drop radius (in millimeters); and N_0, Λ, c, and d are empirical constants determined from the measured distributions.

The three most often referenced distributions are those of Laws and Parsons (ref. 8), Marshall and Palmer (ref. 9), and Joss et al. (ref. 10). The Laws and Parsons distribution was measured directly in tabular form for discrete rain rate values from 0.25 to 150 mm/hr; the Marshall-Palmer and Joss distributions were obtained from radar measurements. The empirical constants of equation (12) are given in table 2.

The Joss distributions are classified into three rain types, while the Marshall-Palmer distribution includes all the measurements in a single distribution, which is similar to the Joss widespread rain case.

TABLE 2.—RAINDROP SIZE DISTRIBUTION EMPIRICAL CONSTANTS

Distribution	N_0, m^{-3} mm^{-1}	Λ, mm^{-1}
Marshall-Palmer	8×10^3	$8.2R^{-0.21}$
Joss et al.:		
Drizzle	30×10^3	$11.4R^{-0.21}$
Rain, widespread	7×10^3	$8.2R^{-0.21}$
Thunderstorm	1.4×10^3	$6R^{-0.21}$

The specific attenuation as given by equation (10) can be expressed as

$$\alpha = 4.343 N_0 \int Q_t(r, \lambda, m) e^{-\Lambda r} dr \tag{13}$$

where Q_t is obtained from equation (11). Equation (13) may be solved numerically for specified values of refractive index, frequency, and drop size distribution. Figure 5 shows the specific attenuation from 1 to 1000 GHz at four specified rain rates obtained by a series expansion solution of the Mie scattering coefficients for the three drop size distributions described. The calculations, made at a rain temperature

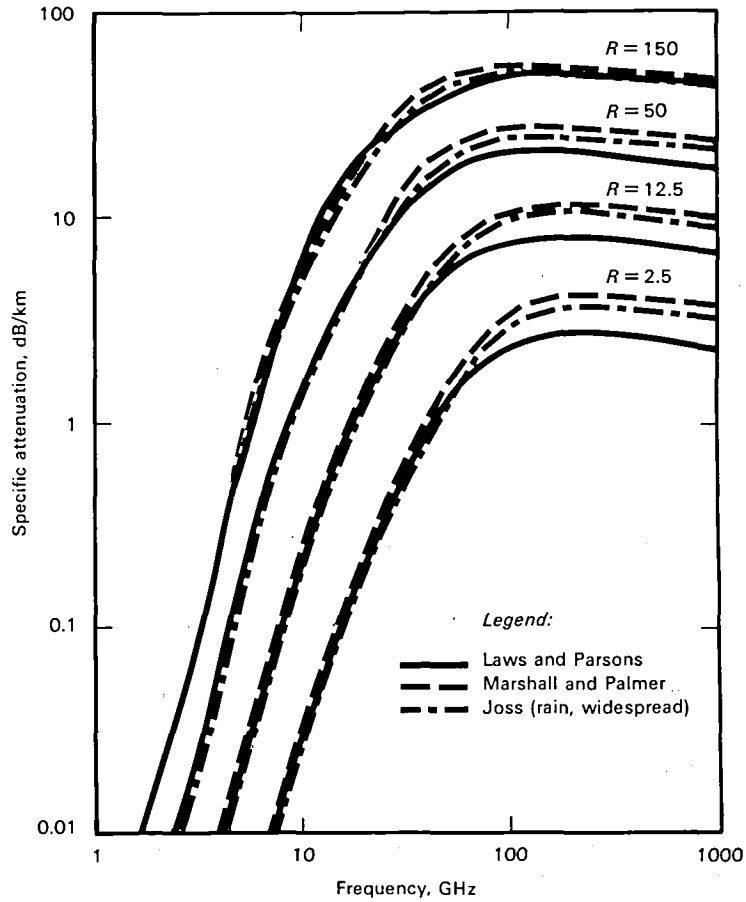

Figure 5.—The specific attenuation of rain from 1 to 1000 GHz at rain rates R of 2.5, 12.5, 50, and 150 mm/hr for the drop size distributions of Laws and Parsons, Marshall-Palmer, and Joss, with a rain temperature of 20° C.

of 20° C, indicate that the attenuation increases rapidly as a function of frequency up to about 60 GHz, then levels off and drops slightly at higher frequencies. There is little difference in the results for the three assumed distributions below 30 GHz; at the higher frequencies the Marshall-Palmer and Joss distributions give higher values because of the greater number of small size drops resulting from the exponential representation of these distributions.

The total rain attenuation for an Earth-satellite slant path is thus obtained by integrating the specific attenuation over the total path L, as given by equations (3) and (13):

$$A = 4.343 \int_0^L \left(N_0 \int Q_t e^{-\Lambda r} dr \right) dx \qquad \text{dB} \tag{14}$$

where the integration over x is taken over the extent of the rain volume in the direction of propagation. In general, both Q_t and the drop size distribution will vary along the propagation path, and these variabilities must be included in the integration process.

Attenuation and Rain Rate

The relationship between rain rate, as measured at Earth's surface, and specific attenuation can be approximated by the equation

$$\alpha = aR^b \qquad \text{dB/km} \tag{15}$$

where a and b are frequency- and temperature-dependent constants that represent the complex behavior of the complete representation of the specific attenuation as given in equation (13). This relatively simple expression for attenuation and rain rate was observed by early investigators directly from empirical observations (refs. 11 and 12); however, more recent studies, most notably that of Olsen, Rogers, and Hodge (ref. 13), have demonstrated the analytical basis for the aR^b expression.

The use of the aR^b expression is included in virtually all present models for the prediction of path attenuation from rain rate, and several sources of tabulations for the a and b coefficients as a function of frequency and temperature are available (refs. 13 to 15). Table 3 presents a listing of the a and b coefficients for several frequencies of interest for satellite communications, as developed by Olsen, Rogers, and Hodge for a 0° C rain temperature. Also listed are examples of specific attenuation at each frequency for rain rates of 10, 50, and 100 mm/hr.

Cloud and Fog Attenuation

Although rain is the most significant hydrometeor affecting radio-wave propagation, the influence of clouds, fog, hail, and snow can also be present on an Earth/space path. Clouds and fog generally consist of water droplets less than 0.1 mm in diameter, allowing the use of the Rayleigh approximation in the calculation of the specific attenuation of clouds and fog up to about 100 GHz. With this approximation cloud attenuation is found to be proportional to the liquid water content rather than the drop size distribution as in the case of rain attenuation.

TABLE 3.—aR^b COEFFICIENTS (MARSHALL-PALMER DROP DISTRIBUTION) FOR THE CALCULATION OF RAIN ATTENUATION AT A RAIN TEMPERATURE OF 0° C

Frequency, GHz	Coefficient		α, dB/km, for R specified in mm/hr		
	a	b	10	50	100
2	0.000345	0.891	0.003	0.011	0.021
4	.00147	1.016	.015	.078	.158
6	.00371	1.124	.049	.30	.657
12	.0215	1.136	.29	1.83	4.02
15	.0368	1.118	.48	2.92	6.34
20	.0719	1.097	.90	5.25	11.24
30	.186	1.043	2.05	11.0	22.7
40	.362	.972	3.39	16.2	31.8
94	1.402	.744	7.78	25.8	43.1

The liquid water content of clouds varies widely, ranging from 0.05 to 0.25 g/m^3 for stratiform to 0.3 to 1.3 g/m^3 for stratocumulus. Peak values exceeding 5 g/m^3 have been found in large cumulus clouds associated with thunderstorms; however, fair weather cumulus clouds generally average less than 1 g/m^3, and cumulonimbus average 2.5 g/m^3. Figure 6 presents the specific attenuation calculated for the range of liquid water content of typical cloud masses, from 0.05 to 2.5 g/m^3. Also shown on the figure for comparison are the specific attenuation values for rain at 1, 2.5, and 10 mm/hr. Typical cumulus clouds range from 2 to 8 km in extent, which is the same order of magnitude expected for the vertical extent of rain on an Earth/space path. The comparisons of figure 6 show that cloud attenuation

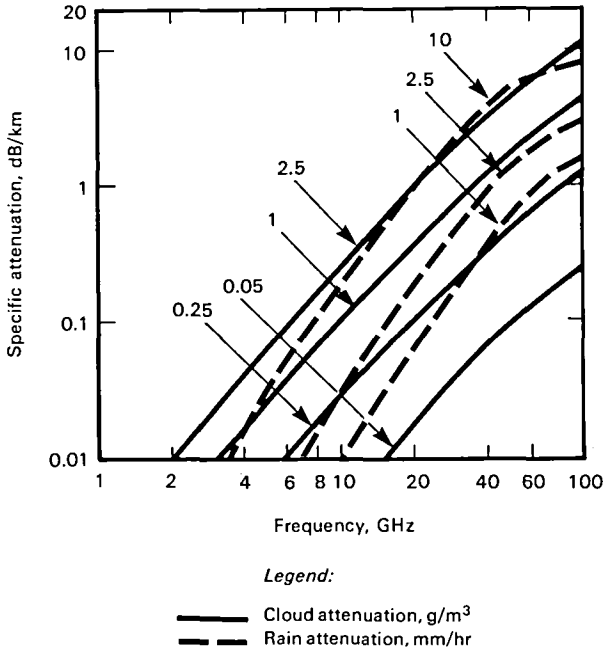

Figure 6.—The specific attenuation for clouds compared to the specific attenuation for rain, Marshall-Palmer distribution, 0° C, from 1 to 100 GHz.

is equivalent to very light rainfall attenuation. During rain that exceeds 10 mm/hr, the rain attenuation will be the dominant factor in the total attenuation experienced on the path. For example, at 20 GHz, the attenuation for a 50 mm/hr rain of 4 km in extent would be 21 dB. A cumulonimbus cloud (2.5 g/m^3) of 4-km extent would result in an added attenuation of 3.5 dB under the same prevalent conditions.

Fog, which results from the condensation of atmospheric water vapor into suspended air droplets, can approach 1 g/m^3 in very dense pockets; however, typically the density ranges around 0.4 g/m^3. Fog layers seldom exceed 50 to 100 m in thickness, hence fog attenuation can usually be considered negligible for radio-wave communications on a slant path.

Slant Path and Elevation Angle Dependence

The total attenuation experienced on a slant path at an elevation angle θ is determined for the specific attenuation α by

$$\begin{aligned} A_\theta &= \frac{L}{\sin\theta}\alpha \\ &= \frac{L}{\sin\theta}aR^b \end{aligned} \tag{16}$$

where L is the extent of the rain volume in the direction of propagation. If the rain rate is not constant over the total path length L, which is generally the case for most communications links, the total attenuation can be found by summing the incremental attenuation for each portion of the path:

$$\begin{aligned} A_\theta &= \frac{L_1}{\sin\theta}aR_1^b + \frac{L_2}{\sin\theta}aR_2^b + \cdots \\ &= \frac{a}{\sin\theta}\sum_{i=1}^{N} L_i R_i^b \qquad \text{dB} \end{aligned} \tag{17}$$

The path attenuation at another elevation angle ϕ can be determined from the path attenuation at angle θ from the equation

$$A_\phi = \frac{\sin\theta}{\sin\phi}A_\theta \tag{18}$$

where the rain is assumed to be horizontally stratified over the interaction region in the vicinity of the ground terminal. The results are strictly valid only for elevation angles above about 10°, where Earth's curvative introduces negligible errors in the surface path projections.

The major problem in the estimation of slant path attenuation is determining the extent of the path length, L and the rain rate profile along that path. A large portion of the significant research accomplished on the effects of rain on satellite communications links has been involved with the determination of techniques and models to characterize the slant path from measurable quantities such as the surface rainfall rate and the 0° C isotherm height. The major results of these modeling techniques

will be reviewed in a later section, after a summary of the measured rain attenuation statistics acquired over the past several years on Earth-satellite links.

Measurement of Rain Attenuation Statistics

Extensive experimental research has been performed on the direct measurement of rain effects on Earth/space paths beginning in the late 1960s with the availability of orbiting propagation beacons on geosynchronous satellites (refs. 16 and 17). The major satellites included the NASA Applications Technology Satellites (ATS 5 and ATS 6); the joint Canadian/U.S. Communications Technology Satellite (CTS); the three COMSAT General COMSTAR satellites (leased to AT&T); the ETS-II, CS, and BSE satellites (Japan); the SIRIO (Italy); and OTS (European Space Agency (ESA)). Table 4 lists the launch date, orbit location, and frequencies of each of the satellites.

Long-term attenuation data are most effectively presented in the form of cumulative distributions, usually on an annual or monthly basis, for communications link design. In this format, link reliability (availability) or exceedance (outage) can be determined and rain margins can be designed into the system to achieve the desired link performance. Figure 7 (from ref. 18), for example, presents cumulative attenuation distributions at 11.7 GHz with the CTS satellite for three consecutive 12-month periods measured at Greenbelt, Md. The elevation angle to the satellite was 29°, and the ground antenna diameter was 4.6 m. The distributions provide an estimate of the rain margins required for a

TABLE 4.—SATELLITES USED FOR PROPAGATION STUDIES ON EARTH/SPACE PATHS

Satellite	Launch date	Orbit location	Frequency, GHz	
			Uplink	Downlink
ATS 5 (NASA)	Aug. 1969	104° W.	31.6	15.3
ATS 6 (NASA)	May 1974	95° W.	[a]13.2	[a]20
		[b]35° E.	[a]17.7	[a]30
		[c]105° W.	—	—
CTS (Canada/U.S.)	Jan. 1976	116° W.	14.0 to 14.3	11.7 to 12.2
COMSTAR (AT&T)	May 1976 (D1)	128° W.	—	[d]19
	July 1976 (D2)	95° W.		[d]28 ± 0.264
	June 1978 (D3)	87° W.		—
ETS-II (Japan)	Feb. 1977	130° E.	—	1.7
				11.5
				34.5
SIRIO (Italy)	Aug. 1977	15° W.	11.6	17.4
CS (Japan)	Dec. 1977	135° E.	27.55 to 30.55	17.75 to 20.25
BSE (Japan)	Apr. 1978	110° E.	14.0 to 14.5	11.7 to 12.2
OTS (ESA)	May 1978	10° E.	14.2 to 14.5	11.5 to 11.8

[a]Frequency applicable at each ATS 6 orbit location.
[b]June 1975.
[c]Nov. 1976.
[d]Frequency applicable for each COMSTAR satellite.

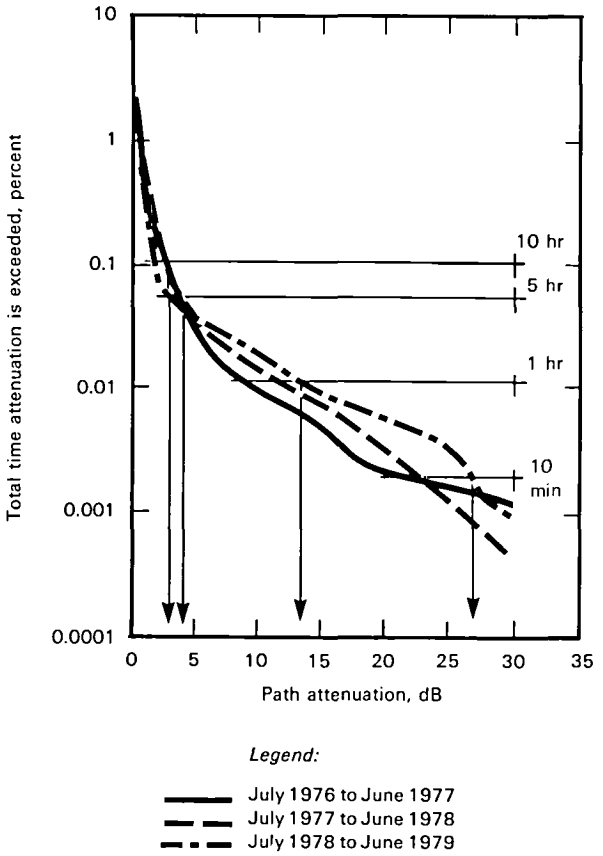

Figure 7.—11.7-GHz attenuation distributions measured at Greenbelt, Md. Elevation angle = 29°; antenna diameter = 4.6 m.

given link reliability, usually expressed in percent, or, equivalently for a given link availability, expressed in hours or minutes. For a 1-hr/yr link availability (0.011 percent), a 13.5-dB margin would have been required for the worst 12-month period of the 3 years measured. Similarly, margins of 3, 4.5, and 27 dB would have been required for 10-hr/yr, 5-hr/yr, or 10-min/yr link outage. A link with 1-hr/yr outage is considered a high-quality link, similar to what is specified for the national telephone system.

Table 5 summarizes the results of annual 11-GHz measurements observed in the United States, Europe, and Japan using the CTS, SIRIO, BSE, and ETS-II satellite beacons at 11.7, 11.6, 11.7, and 11.5 GHz, respectively (refs. 18 to 26). The U.S. stations tend to exhibit a more severe attenuation than the European stations for a given percent outage, which is to be expected because the rain conditions are more severe in the U.S. regions, particularly for thunderstorm occurrence periods, which account for most of the attenuation observed below about 0.05 percent outage. The more limited Japanese data tend to fall somewhere between the U.S. and European results. The mean attenuation for a 0.01-percent outage (53 min/yr) is 11.2 dB for the U.S. sites, 4 dB for the European sites, and 5.8 dB for Japan. Some variability between locations is to be expected because of the different observation periods and elevation angles; however, the data exhibit a fairly consistent trend and give a good indication of what could be expected on an operational communications link.

The five U.S. locations have acquired nearly 25 station-years of 11.7-GHz satellite attenuation data, and the long-term attenuation distributions are shown on figure 8. The multiyear distributions demonstrate the "dual mode" characteristic of rain-induced attenuation: the low attenuation values

TABLE 5.—SUMMARY OF 11-GHz ANNUAL ATTENUATION MEASUREMENTS

Location	Elevation angle, deg	Time period	Attenuation, dB, for given outage specified in percent							Reference
			1	0.5	0.1	0.05	0.01	0.005	0.001	
Waltham, Mass.	24	Feb. 1977 to Jan. 1978	<1	<1	2.5	4	10.5	14.5	[a]23	19
		Feb. 1978 to Jan. 1979	<1	<1	1.5	2.8	8.5	11	15.3	
Holmdel, N.J.	27	June 1976 to June 1977	<1	<1	3	5	13.5	—	—	20
		June 1977 to June 1978	<1	<1	3	5	13.5	19.5	—	
		June 1978 to June 1979	<1	<1	2.5	3.8	9.2	12.2	29	
Greenbelt, Md.	29	July 1976 to June 1977	<1	<1	1.8	3.2	8.8	14.5	<30	18
		July 1977 to June 1978	<1	1	2.1	3.8	12	18	26.4	
		July 1978 to June 1979	<1	<1	1.8	3.2	14	21	29.2	
Blacksburg, Va.	33	Jan. 1977 to Dec. 1977	2	2.5	4	5	13	16.5	24	21
		Jan. 1978 to Dec. 1978	2	2.7	3.7	4.3	6.8	8.6	13	
Austin, Tex.	49	Feb. 1978 to Jan. 1979	<1	1	3	5.5	13	18	23	22
Nederhorst Den Berg, Netherlands	27.5	Aug. 1975 to Oct. 1975[b] and Apr. 1976 to June 1977[c]	.8	1	1.5	1.8	3.2	3.8	6	23
Munich, Germany	29	Jan. 1978 to Dec. 1978[d]	3	4	6.8	—	—	—	—	24
Fucino, Italy	30	Jan. 1978 to Dec. 1978	1	1	2	2.5	4	5.2	12	25
Lario, Italy	30	Jan. 1978 to Dec. 1978	1	1	2	2.7	4.8	6.8	13.2	25
Kashima, Japan	[e]38	Aug. 1978 to June 1979	—	—	2.2	3	5.3	6.5	11	26
	[f]47	May 1977 to Apr. 1978	1	1.2	2.5	3.5	6.2	7.5	15.5	

[a]Extrapolated from measured data.
[b]Includes radiometer data.
[c]8100 hr total.
[d]91.2 percent coverage.
[e]BSE.
[f]ETS-II.

(below about 0.05 percent per year) are caused by stratiform rainfall, and the higher attenuation "tails" of the distribution are produced by the more severe convective rain usually associated with thunderstorm activity. The resulting rain margins for the four stations that have nearly identical

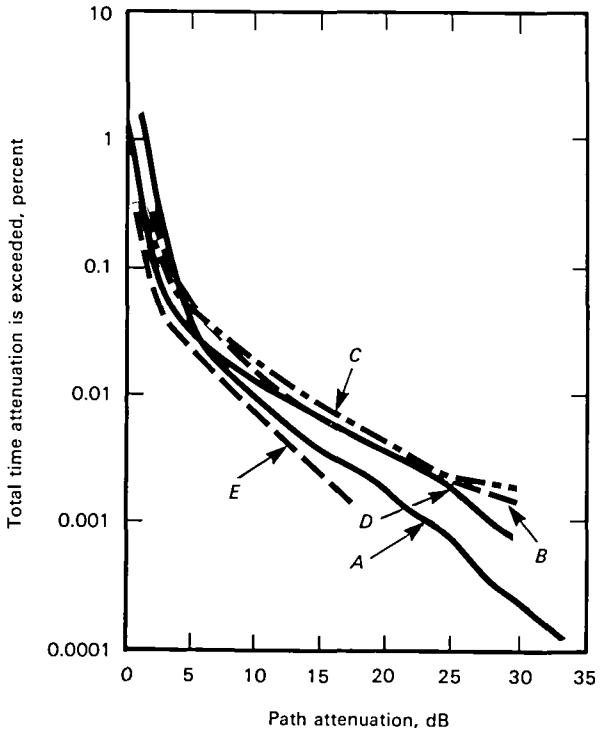

Legend:

A	Blacksburg, Va.; 36 months: June 1976 to July 1979, 33°	*D*	Greenbelt, Md.; 36 months: July 1976 to June 1979, 29°
B	Holmdel, N.J.; 36 months: May 1976 to Apr. 1979, 27°	*E*	Waltham, Mass.; 29 months: Feb. 1977 to June 1979, 24°
C	Austin, Tex.; 36 months: June 1976 to June 1979, 49°		

Figure 8.—Multiyear 11.7-GHz attenuation distributions measured in the United States.

elevation angles around 30° are 2.5 ± 1 dB, 11.2 ± 2.2 dB, and 14.5 db ± 3 dB for link reliabilities of 99.9, 99.99, and 99.995 percent respectively.

A large data base of rain attenuation measurements in the 20- to 30-GHz bands also is available in the United States, beginning with measurements in 1974 using the ATS 6 satellite. Tables 6 (refs. 17, 21, 27, and 28) and 7 (refs. 17, 21, and 27 to 29) present lists of annual attenuation statistics at 20 and 30 GHz, respectively, for several locations and elevation angles ranging from 18.5° to 54.4°. The attenuation is, as expected, more severe with increasing frequency, reaching very high levels at 30 GHz for outages of 0.05 percent and less. The mean attenuations at 0.5 percent outage are 2.7 and 5.7 dB for 20 and 30 GHz, respectively, and for 0.1 percent outage, are 8.7 and 15.8 dB, respectively.

The experimental measurements of rain attenuation have to be evaluated with an awareness of the wide variabilities that exist in weather conditions, elevation angle, and measurement techniques. Even with these limitations, however, some general observations on the magnitude of rain attenuation on space communications are apparent. Based on the nearly 30 station-years of measurements in the temperate continental climate regions of the United States, the link reliabilities given in table 8 should be achievable for the given rain margin.

TABLE 6.—SUMMARY OF 20-GHz ANNUAL ATTENUATION MEASUREMENTS

Location	Elevation angle, deg	Time period	Attenuation, dB, for given outage specified in percent							Reference
			1	0.5	0.1	0.05	0.01	0.005	0.001	
Holmdel, N.J.	18.5	June 1976 to June 1977	2.5	4	12	18	>40	—	—	27
Grant Park, Ill.	27.3	July 1976 to June 1977	—	3	9.5	19	>30	—	—	27
Palmetto, Ga.	29.9	June 1976 to July 1977	—	3	10	18	>28	—	—	27
Waltham, Mass.	35.3	Jan. 1978 to Dec. 1978[a]	<2	<2	3.5	5.2	29	—	—	28
Holmdel, N.J.	38.6	May 1977 to May 1978	1	2.5	6.5	9	22	33	>44	27
Grant Park, Ill.	41.8	Aug. 1977 to Aug. 1978	—	2.5	9	17	>30	—	—	27
Blacksburg, Va.	45	Jan. 1978 to Dec. 1978	1.7	2.4	4.9	5.7	11.3	15.6	24.5	21
		Jan. 1979 to Dec. 1979[b]	2	2.5	5	7	13.5	18	25	
Rosman, N.C.	45	Jan. 1974 to Dec. 1974	2	3.5	10	11	—	—	—	17
Palmetto, Ga.	49.5	Aug. 1977 to Aug. 1978	—	2	9	17	>30	—	—	27
Austin, Tex.	52	Oct. 1978 to Oct. 1979	1	1.8	7.2	12.2	23	24	—	17
Tampa, Fla.	54.4	Jan. 1978 to Dec. 1978	—	<2	21	>30	—	—	—	28
		Jan. 1979 to Dec. 1979	<1	4.6	>30	—	—	—	—	

[a]Excluding September.
[b]Excluding February.

The results given in table 8 are based on an upper bound margin of at least one standard deviation above the mean value calculated for all the available data in each frequency band. In operational space communications systems, power margins of 6 to 10 dB can be achieved with a reasonable system design, but margins above 10 to 15 dB can be costly and difficult to achieve. From the measured results it can be seen that a 99.5-percent link reliability is a reasonable objective at any of the three frequency bands; however, reliabilities of 99.95 percent or better at 20 GHz and 99.9 percent or better at 30 GHz will require other techniques, such as site diversity or spot beams, in addition to the basic power margin designed into the link.

Rain Attenuation Prediction Methods

The evaluation of rain attenuation for satellite link system design requires a detailed knowledge of the attenuation statistics for each ground terminal location at the specific frequency of interest. Direct

TABLE 7.—SUMMARY OF 30-GHz ANNUAL ATTENUATION MEASUREMENTS

Location	Elevation angle, deg	Time period	Attenuation, dB, for given outage specified in percent							Reference
			1	0.5	0.1	0.05	0.01	0.005	0.001	
Grant Park, Ill.	27.3	July 1976 to June 1977	—	6.5	17	>30	—	—	—	27
Palmetto, Ga.	29.9	June 1976 to July 1977	—	7.5	20	>28	—	—	—	27
Waltham, Mass.	35.3	Jan. 1978 to Dec. 1978[a]	<2	2.6	7.5	11	>30	—	—	28
Holmdel, N.J.	38.6	May 1977 to May 1978	3.5	5.5	14.5	21.5	44	—	—	27
Wallops Is., Va.	41.6	Apr. 1977 to Mar. 1978	2.3	4	12.5	25	—	—	—	29
Grant Park, Ill.	41.8	Aug. 1977 to Aug. 1978	—	5	20	>30	—	—	—	27
Blacksburg, Va.	45	Jan. 1978 to Dec. 1978	5	6.4	11.8	14.9	24	—	—	21
		Jan. 1979 to Dec. 1979[b]	4	5	8.5	12	25	35	—	
Rosman, N.C.	45	Jan. 1974 to Dec. 1974	3.5	6	22	25	—	—	—	17
Palmetto, Ga.	49.5	Aug. 1977 to Aug. 1978	—	6.5	18	>30	—	—	—	27
Austin, Tex.	52	Oct. 1978 to Oct. 1979	1.5	3.6	17	27.5	—	—	—	17

[a]Excluding September.
[b]Excluding February.

long-term measurements of path attenuation for all potential ground terminal locations in an operational domestic satellite network are not feasible. Over the past several years extensive efforts have been undertaken to develop reliable techniques for the prediction of path rain attenuation for a

TABLE 8.—ACHIEVABLE LINK RELIABILITIES

Link reliability, percent	Outage, hr/yr	Margin, dB, for given frequencies specified in GHz		
		11	20	30
99.5	44	1	3	6
99.9	8.8	3	10	20
99.95	4.4	5	20	>30
99.99	.88	15	>30	—

given location and frequency, and the recent availability of satellite beacon measurements has provided for the first time a data base for validation and refinement of the prediction models. In this section several of the more promising prediction techniques are reviewed.

Virtually all the prediction techniques proposed use surface-measured rain rate as the statistical variable and assume the aR^b relationship described earlier to determine rain-induced attenuation. In general, the prediction models can be expressed in the form

$$A = aR^bL(R) \qquad \text{dB} \tag{19}$$

where R is the rain rate, a and b are the frequency-dependent constants described by equation (15), and $L(R)$ is an "effective" path length parameter, usually a specified function of R. The path length parameter $L(R)$ is the coupling function that develops an attenuation distribution from a specified rain rate distribution, through equation (19). The major difference between the various rain attenuation prediction methods available is in the rationale used to develop the path length parameter $L(R)$.

Much of the early work that led to the development of rain attenuation models was focused on empirical models that described rain rate distributions as a function of location. The International Radio Consultative Committee (CCIR) adopted at its April 1972 meeting in Geneva a procedure to estimate the cumulative distribution of rainfall based on the concept of rain climate zones (ref. 30). The procedure, as later modified (ref. 31), consists of a global map dividing the land areas of Earth's surface into five climate regions and provides an averaged annual rain rate distribution for each region.

Rice-Holmberg Rain Model

A global surface rainfall model developed from extensive long-term rainfall statistics from over 150 locations throughout the world was developed by Rice and Holmberg (ref. 32). The Rice-Holmberg model constructs the rainfall rate distribution from two types of rain, "thunderstorm rain" and "all other rain." Each mode is modeled by exponentials, and the sum of the two modes produces the total distribution. The percent of an average year for which the rainfall rate exceeds R mm/hr at a medium location is given by

$$P(R) = \frac{M}{87.6}[0.03\beta e^{-0.03R} + 0.2(1-\beta)(e^{-0.258R} + 1.86e^{-1.63R})] \qquad \text{percent} \tag{20}$$

where

M = average annual rainfall accumulation, in millimeters

M_1 = average annual accumulation of thunderstorm rain, in millimeters

$$\beta = \frac{M_1}{M}$$

R = clock minute rainfall rate, in millimeters per hour

Global maps for M, M_1, and β are provided in the model, or, where available, directly measured data

can be used. The Rice-Holmberg model has been shown to provide very good agreement for several locations in the United States where long-term rain data have been measured directly.

Dutton-Dougherty Attenuation Prediction

The global surface rain rate method of Rice-Holmberg was extended by Dutton and Dougherty to include an attenuation prediction based on meteorological considerations of the propagation path (refs. 33 and 34). The Dutton-Dougherty (DD) model expresses the clock minute rainfall rate distribution for an average year in three segments:

$$P(R) = 0.0114(T_{11} + T_{21}) \exp(-R/R_1') \qquad R < 5 \text{ mm/hr} \qquad \text{percent} \qquad (21a)$$

$$P(R) = 0.0114 T_{21} \exp[-(R/R_{21})^{1/4}] \qquad 5 \leq R \leq 30 \text{ mm/hr} \qquad \text{percent} \qquad (21b)$$

$$P(R) = 0.0114 T_{11} \exp(-R/\bar{R}_{11}) \qquad R > 30 \text{ mm/hr} \qquad \text{percent} \qquad (21c)$$

where T_{11}, T_{21}, R_1', and $\bar{R}_{11}$ are linear combinations of M, β, and $D = 24 + 3M$ determined from the regression equations:

$$T_{21} = b_{11}M + b_{21} \pm s_2 \qquad (22)$$

$$R_1 = b_{31}M + b_{41}\beta + b_{51}D + b_{61} \pm s_3 \qquad (23)$$

$$\bar{R}_{11} = \frac{\beta M}{T_{11}}$$

$$= a_{11}M + a_{21}\beta + a_{31}D + a_{41} \pm s_1 \qquad (24)$$

The DD attenuation distribution prediction is developed from the rain rate distribution through the following assumptions:

(1) Marshall-Palmer drop-size distribution (ref. 9)
(2) Storm height distribution of Grantham and Kantor (ref. 35)
(3) Vertical dependence of liquid water content from Dutton (ref. 36)
(4) Specific attenuation coefficients, $a(f)$ and $b(f)$, of Crane (ref. 37)

The DD model predicts total atmospheric attenuation; i.e., clear air, clouds, and precipitation. Figure 9 presents a comparison of the DD prediction curves with measured annual attenuation data for four locations at 11.7 and 19 GHz. The DD method provides a mean prediction (50 percent confidence limit) and upper and lower bounds (±5 and ±0.5 percent from the mean prediction (ref. 38)). The solid curves labeled 1 through 5 on figure 9 represent these predictions. The DD model is seen to provide a very good prediction for the 19-GHz data for Blacksburg, Va. (fig. 9(*d*)). The 6 years of 11.7-GHz measurements at Greenbelt and Holmdel fall above the mean curves for attenuation values exceeding 6 dB, but remain within the 99.5 percent confidence limit up to about 15 dB or 0.01 percent, which is the upper limit of the published DD model. The data from Austin (fig. 9(*c*)) extend above the range of the prediction bounds throughout the measurement range.

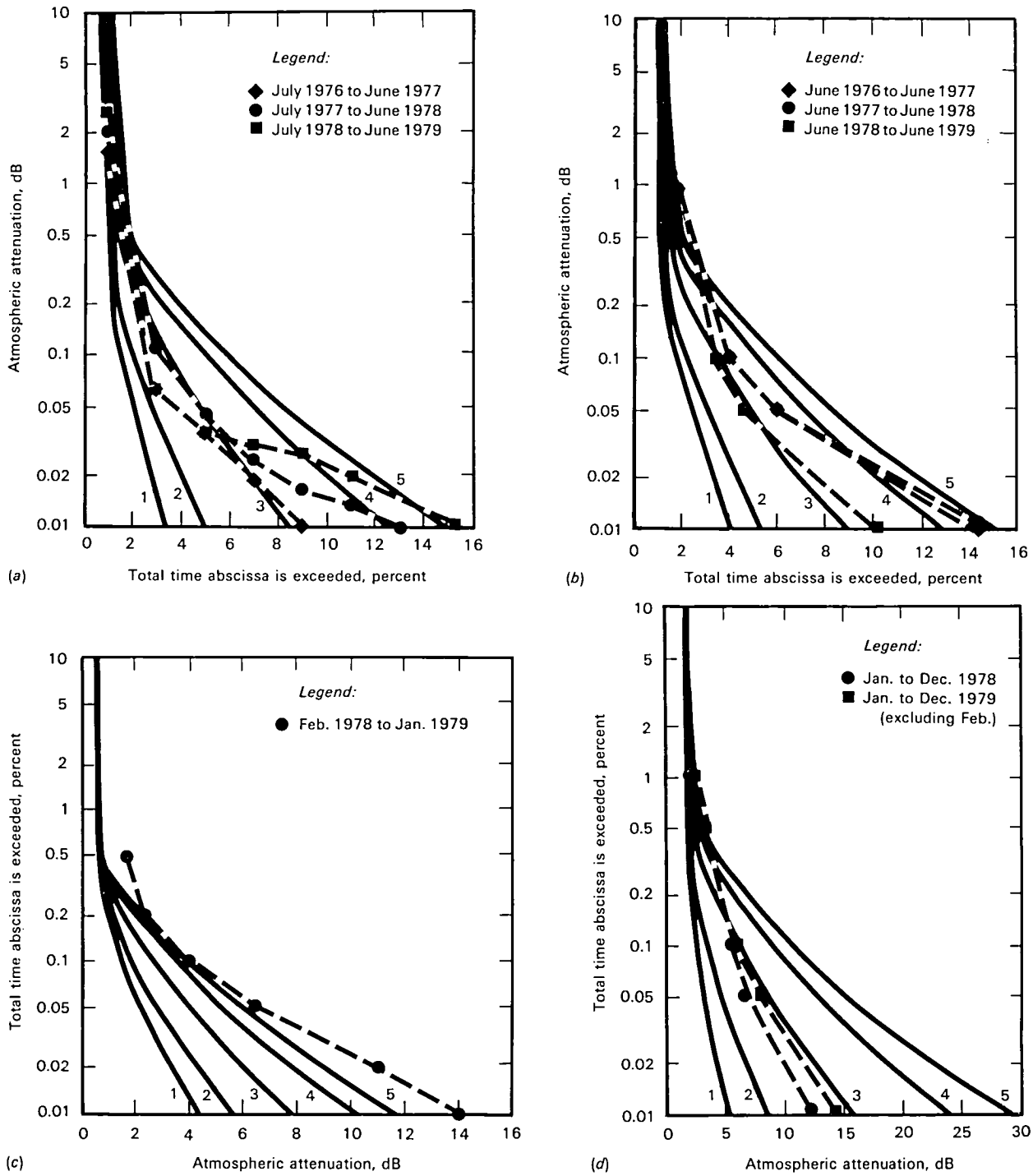

Figure 9.—Comparison of the Dutton-Dougherty attenuation prediction with measured data. Curve 1 represents the 0.5-percent confidence limit, curve 2 represents the 5-percent confidence limit, curve 3 represents the mean prediction, curve 4 represents the 95-percent confidence limit, and curve 5 represents the 99.5-percent confidence limit. (*a*) Greenbelt, Md. (prediction for Washington, D.C.); 11.7 GHz; elevation angle = 29°. (*b*) Holmdel, N.J. (prediction for Trenton, N.J.); 11.7 GHz; elevation angle = 27°. (*c*) Austin, Tex.; 11.7 GHz; elevation angle = 45°. (*d*) Blacksburg, Va. (prediction for Roanoke, Va.); 19 GHz; elevation angle = 19°.

At the present time the DD model computer program is not available for general application, and the prediction curves available have been generated by the authors.

Lin Model

An empirical method for estimating rain-induced outage probabilities on radio-wave paths was developed by Lin (refs. 39 and 40). The Lin method is based on a 5-min point rain rate rather than the 1 min or less rain gage integration times of other prediction techniques. Two arguments are presented to justify the use of the 5-min averaging time. First, the available long-term rain rate data published by the National Climate Center have minimum integration times of 5 min, and attempts to estimate shorter times from the original strip chart data produce significant uncertainty. Second, the 5-min averaging time effectively develops a path average rain rate distribution from a point rain rate distribution; i.e., the spatial average of the rain rate along the radio-wave path can be represented by a 5-min average of the rain rate at a single point on the path.

The relationship between path attenuation and 5-min rain rate was determined empirically from measurements on nine 11-GHz terrestrial paths, 5 to 43 km in length, at five locations in the United States. The resulting equation is

$$A_L = aR_5^b L \left[\frac{1}{1 + L/\bar{L}(R_5)} \right] \tag{25}$$

where R_5 is the 5-min point rain rate, a and b are the frequency dependent constants described by equation (15), and L is the terrestrial path length. The term in brackets is a "path length correction factor" chosen to represent the empirical ratio between the 5-min point rain rate and the radio path average rain rate at the same probability (ref. 40).

The function $L(R_5)$ was determined from the terrestrial path measurements:

$$L(R_5) \cong \frac{2636}{R_5 - 6.2} \qquad \text{km} \tag{26}$$

Lin extended the terrestrial path results to a slant path at an elevation angle θ by geometric considerations similar to those employed in equation (16) to obtain

$$L = \frac{H - G}{\sin \theta} \tag{27}$$

where H is the long-term average 0° isotherm height, assumed by Lin to be 4 km for eastern U.S. locations, and G is the ground terminal elevation above sea level.

The resulting prediction equation for slant path rain attenuation is then

$$A_\theta = aR_5^b \left[\frac{2636}{R_5 - 6.2 + 2636 \sin \theta/(4 - G)} \right] \qquad \text{dB} \tag{28}$$

The term in brackets corresponds to the Lin effective path length parameter $L(R)$ defined in equation (19).

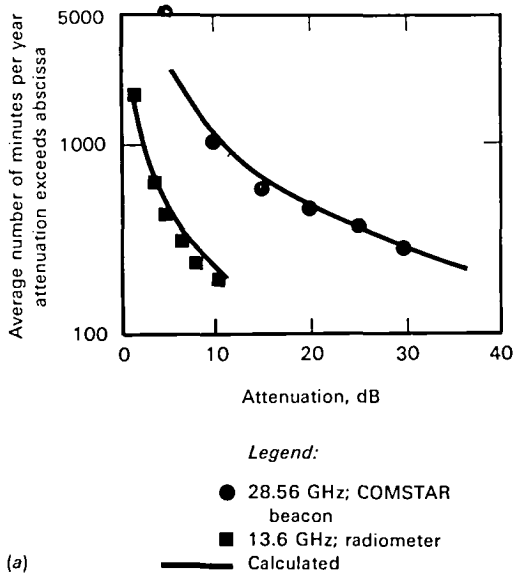

(a)

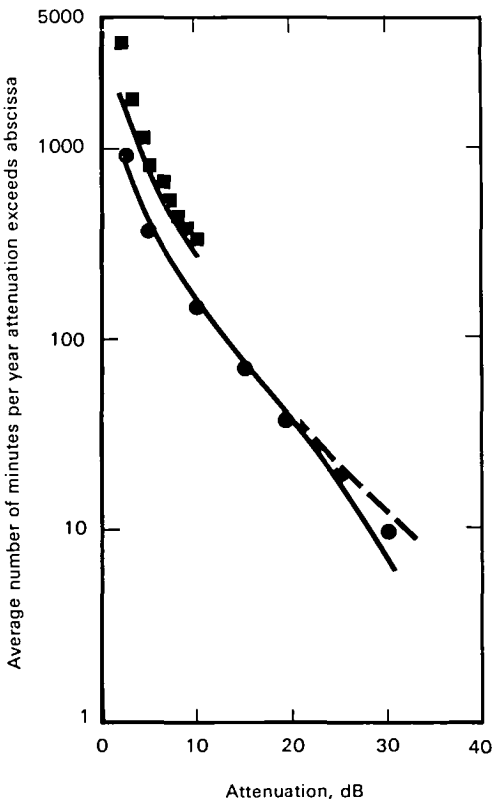

(b)

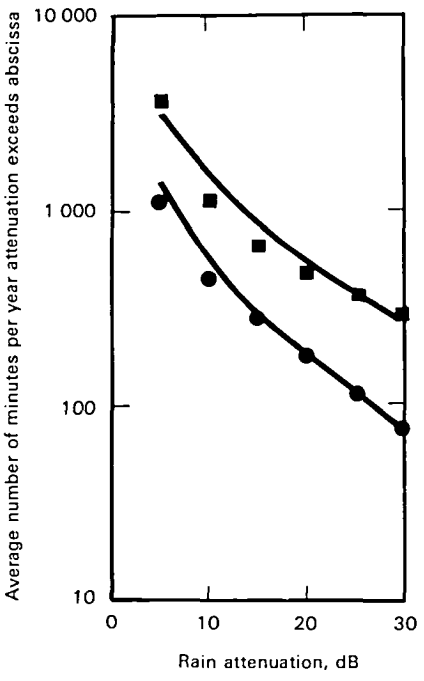

(c)

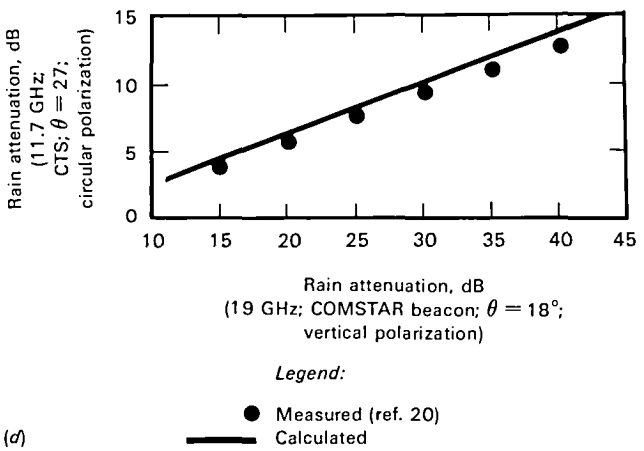

(d)

Figure 10.—Comparison of the Lin attenuation prediction model with measured data (from Lin (ref. 40)). (*a*) Grant Park, Ill.; July 1976 to June 1977; elevation angle = 27.3°; ground elevation = 0.2 km. (*b*) Holmdel, N.J.; ground elevation: negligible. (*c*) Palmetto, Ga.; COMSTAR beacon data from Aug. 1977 to Aug. 1978; elevation angle = 49.5°; ground elevation = 29 km. (*d*) Crawford Hill, N.J.; July 29 to Aug. 27, 1976.

Figure 10 presents a comparison of the attenuation prediction model as calculated by Lin with measured attenuation statistics for four location in the eastern United States at frequencies from 11.7 to 28.56 GHz. The prediction curves are seen to give very good agreement with the measured data throughout the range of comparison.

Crane Global Attenuation Model

A rain attenuation prediction model recently developed by R. K. Crane provides, for the first time, a completely self-contained prediction procedure that is applicable on a global basis (refs. 41 and 42). The global model is based upon the use of geophysical data to determine the surface point rain rate, point-to-path variations in rain rate, and the height dependency of attenuation given the surface point rain rate or the percentage of the year the attenuation value is exceeded. The model also provides estimates of the expected year-to-year and station-to-station variations of the attenuation prediction for a given percent of the year.

Surface point rain rate data for the United States and global sources were used to produce 10 rain rate climate regions for the land and water surface areas on Earth. The boundaries for each climate region were adjusted for expected variations in terrain, storm type, storm motion, and atmosphere circulation. Figure 11 shows the resulting global map of the eight basic climate regions, including the ocean areas. The continental United States climate region (region D) was further subdivided into regions D_1, D_2, and D_3 (see fig. 12) because of the extensive amount of surface rain data available and the wide variations observed throughout the region. The rain rate distributions for all 10 regions are listed in table 9.

The Crane model relates the surface point rain rate R_p to a path-averaged rain rate R through an effective path average factor determined empirically from terrestrial measurements of rain rate at path lengths up to 22.5 km. The resulting relationship was modeled by a power law expression:

$$\bar{R} = \gamma(D) R_p^{1+\delta(D)} \tag{29}$$

where D is the horizontal path length and γ and δ are determined from a best-fit analysis of the terrestrial path data. Relative path profile curves for rain rate as a function of D were determined by numerically differentiating γ and δ, then represented by two exponential functions, over the range of D from 0 to 22.5 km. The resultant piecewise exponential expression for integrated attenuation for a slant path at an elevation angle θ as a function of the point rain rate R_p is

$$A(R_p, D) = \frac{aR_p^b}{\cos\theta} \frac{e^{UbD} - 1}{Ub} \qquad 0 < D \leq d \tag{30}$$

$$A(R_p, D) = \frac{aR_p^b}{\cos\theta} \left(\frac{e^{Ubd} - 1}{Ub} - \frac{X^b e^{Ybd}}{Yb} + \frac{X^b e^{YbD}}{Yb} \right) \qquad d < D \leq 22.5 \quad \text{km} \tag{31}$$

where U, X, and Y are empirical constants that depend on R_p. These constants are

$$U = \frac{1}{d} \ln Xe^{Yd} \tag{32}$$

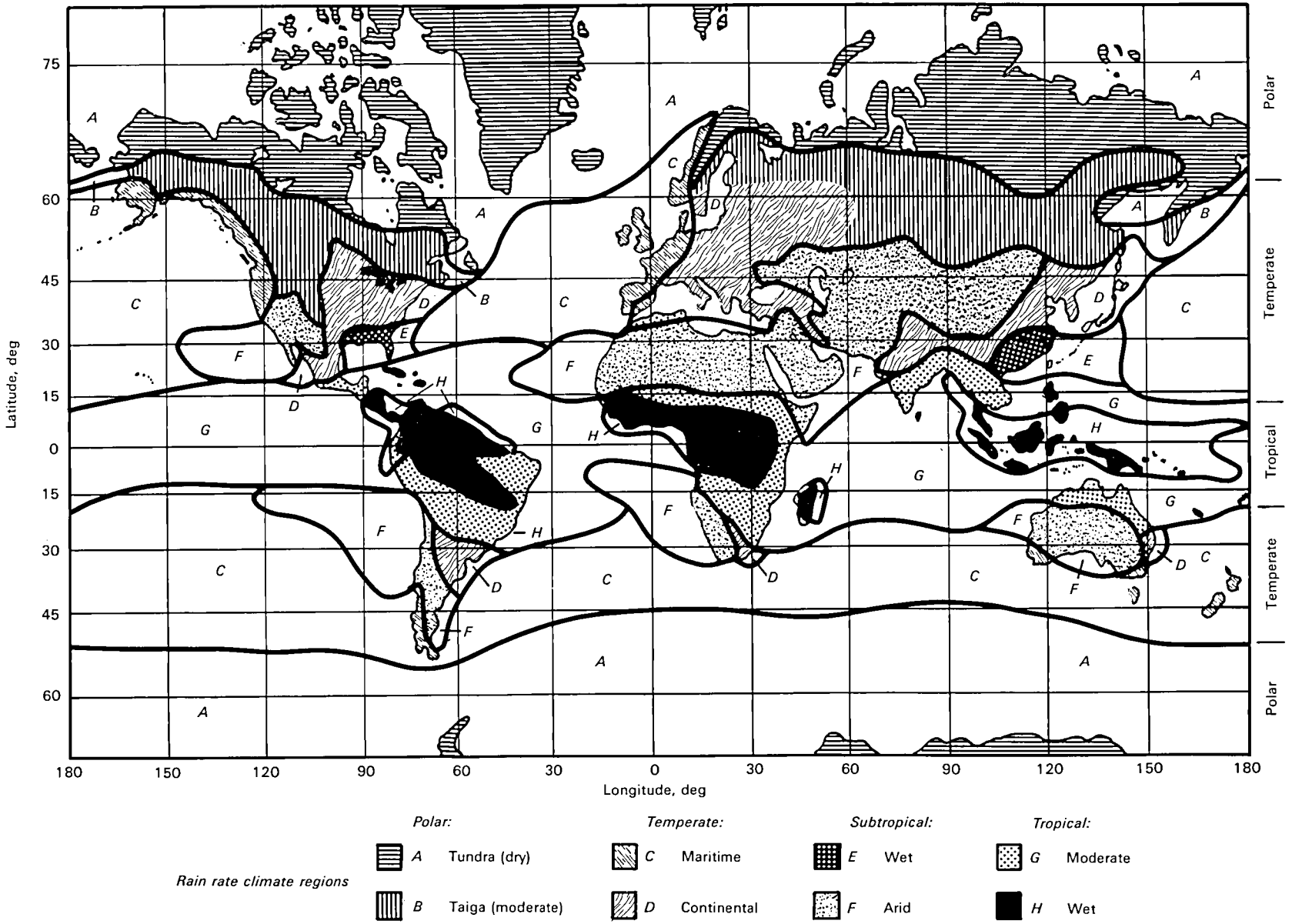

Figure 11.—Rain rate climate regions for the global rain attenuation model.

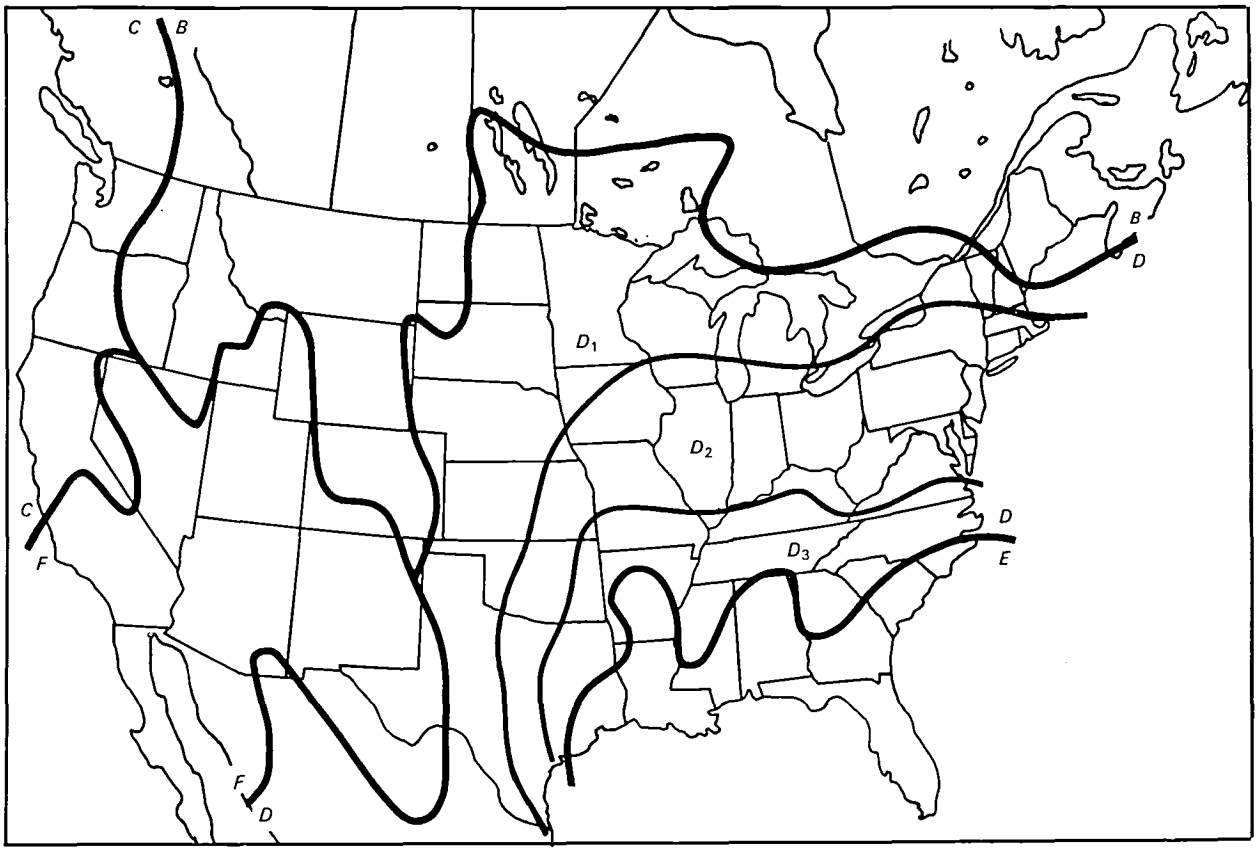

Figure 12.—Rain rate climate regions for the continental United States, showing the subdivisions of region *D*.

TABLE 9.—POINT RAIN RATE DISTRIBUTION VALUES FOR THE GLOBAL MODEL

Rain rate exceeded, percent of year	Point rain rate distribution values (mm/hr) per rain climate region										Minutes per year	Hours per year
	A	*B*	*C*	D_1	D_2	D_3	*E*	*F*	*G*	*H*		
0.001	28	54	80	90	102	127	164	66	129	251	5.3	0.09
.002	24	40	62	72	86	107	144	51	109	220	10.5	.18
.005	19	26	41	50	64	81	117	34	85	178	26	.44
.01	15	19	28	37	49	63	98	23	67	147	53	.88
.02	12	14	18	27	35	48	77	14	51	115	105	1.75
.05	8	9.5	11	16	22	31	52	8.0	33	77	263	4.38
.1	6.5	6.8	72	11	15	22	35	5.5	22	51	526	8.77
.2	4.0	4.8	4.8	7.5	9.5	14	21	3.8	14	31	1 052	17.5
.5	2.5	2.7	2.8	4.0	5.2	7.0	8.5	2.4	7.0	13	2 630	43.8
1.0	1.7	1.8	1.9	2.2	3.0	4.0	4.0	1.7	3.7	6.4	5 260	87.66
2.0	1.1	1.2	1.2	1.3	1.8	2.5	2.0	1.1	1.6	2.8	10 520	175.3

$$X = 2.3R_p^{-0.17} \tag{33}$$

$$Y = 0.026 - 0.03 \ln R_p \tag{34}$$

$$d = 3.8 - 0.6 \ln R_p \tag{35}$$

The vertical variation of rain rate is accounted for by assuming that R is constant from the surface to the 0° isotherm height, but the 0° isotherm is expressed as a variable that is a function of station location (latitude) and the probability of occurrence, as shown on figure 13.

The annual attenuation distribution is generated from equations (30) and (31) as follows: (1) select the rain rate distribution for the desired location from the rain climate region maps and table 9; (2) determine the surface projected path length for each percent of the year value from

$$D = \frac{H(P) - G}{\tan \theta} \qquad \theta \geq 10° \qquad d \leq 22.5 \qquad \text{km} \tag{36}$$

where $H(P)$ is the 0° isotherm height found from figure 13, G is the ground terminal elevation above sea level, and θ is the elevation angle; and (3) calculate the slant path attenuation for each percent of the year value for equations (30) and (31), with the a and b coefficients selected for the frequency of interest.

Upper and lower bounds on the annual attenuation distribution prediction were developed by combining the statistical variances of each step in the model development. Figure 14 presents the global model mean prediction and bounds for several locations and frequencies, compared with measured attenuation distributions at those locations. All of the predictions show excellent correlation with the measured data, except for the Blacksburg, Va., distributions at 28.56 GHz. The global model develops a prediction curve down to 0.001 percent and tends to reproduce the tails of the curve consistently well. The sharp dropoffs in the measured data from Austin, Tex. (fig. 14(*e*)), are most likely caused by the noise characteristics of the receiver systems as the rain attenuation drives the receiver signal level down to its threshold.

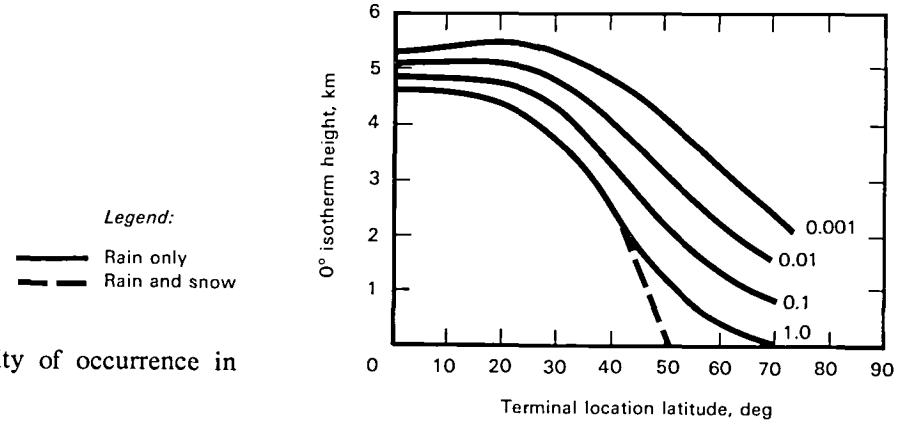

Figure 13.—Annual probability of occurrence in percent.

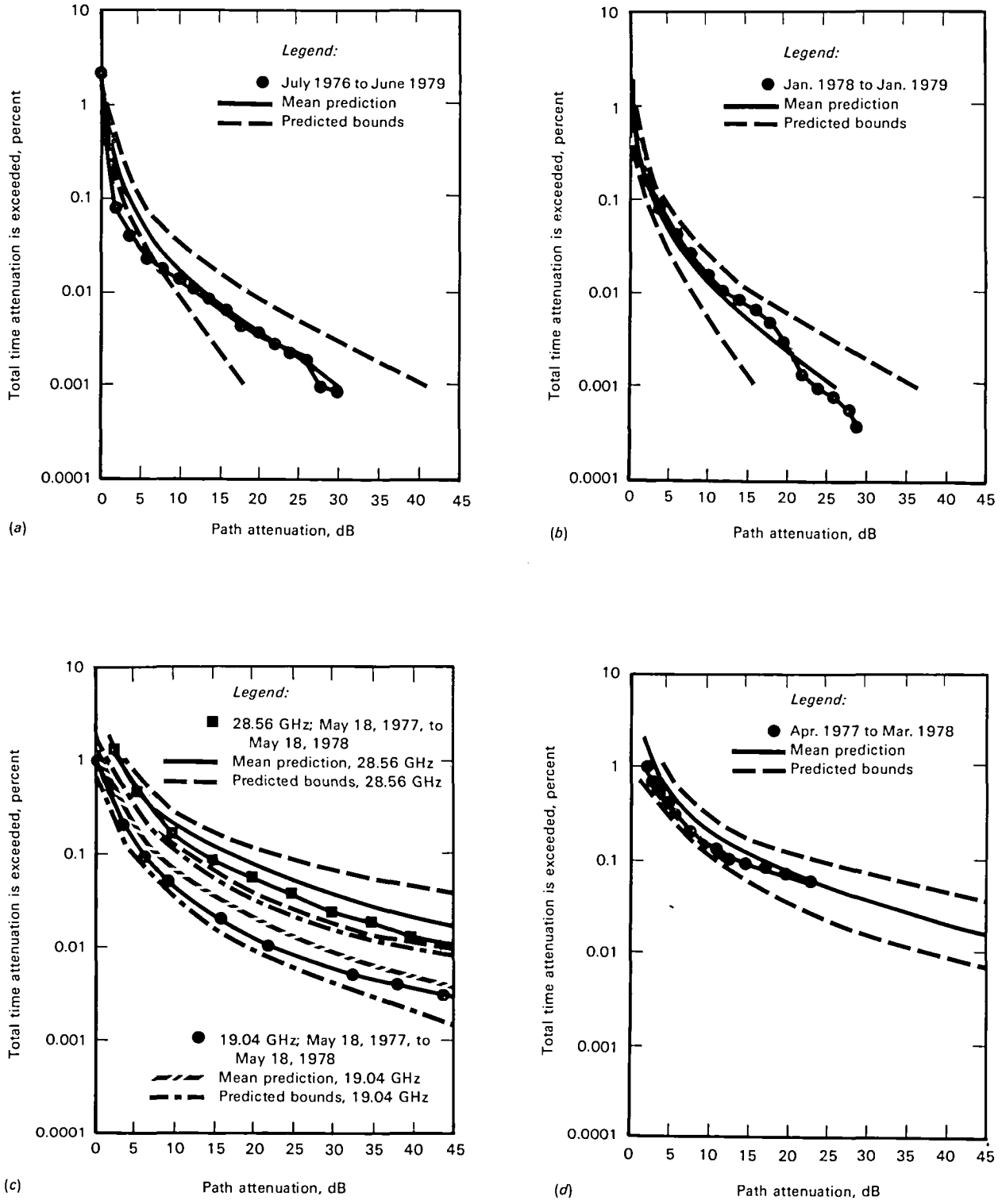

Figure 14.—Comparison of the Crane global attenuation prediction model with measured data. The predicted bounds curves represent ±1 standard deviation about the mean curve. (*a*) Greenbelt, Md.; 11.7 GHz; elevation angle = 29°. (*b*) Austin, Tex.; 11.7 GHz; elevation angle = 49°. (*c*) Holmdel, N.J.; elevation angle = 38.6°. (*d*) Wallops Island, Va.; 28.56 GHz; elevation angle = 41.6°.

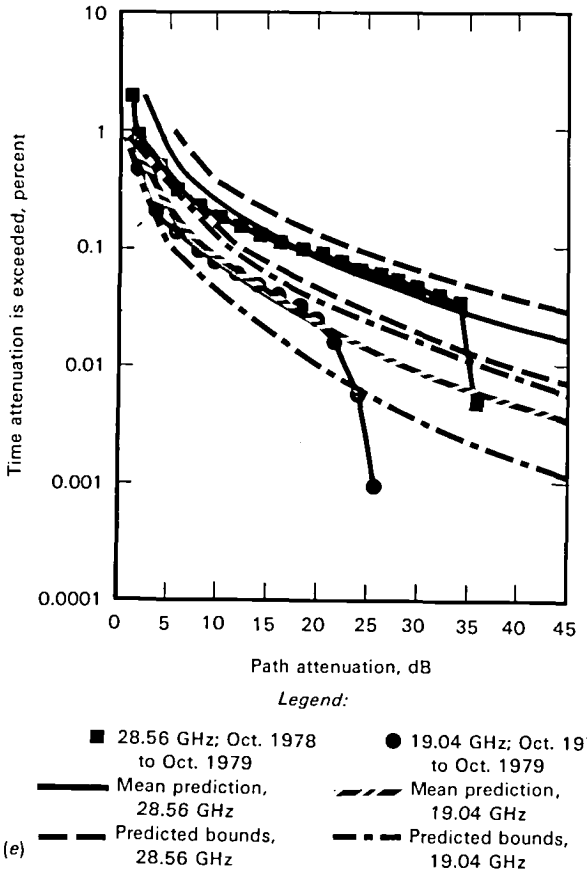

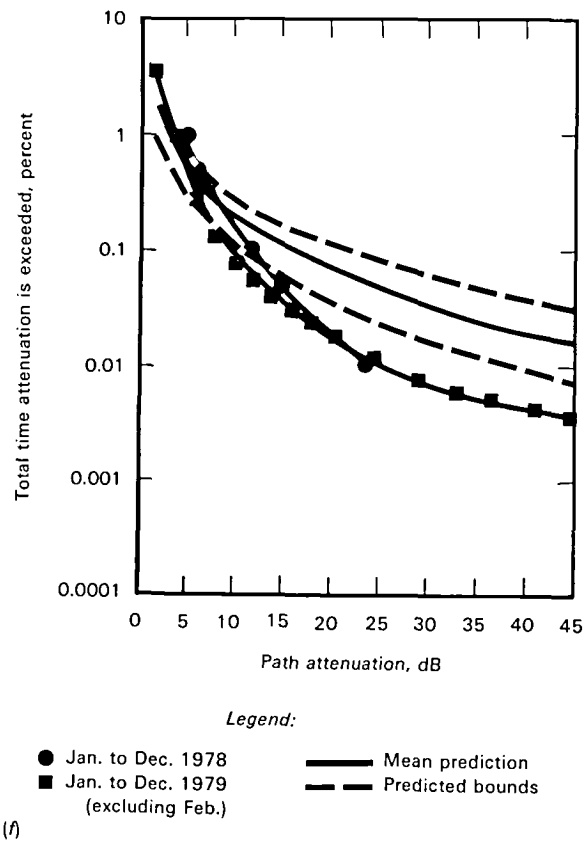

Figure 14 (concluded).—(*e*) Austin, Tex.; elevation angle = 45°. (*f*) Blacksburg, Va.; 28.56 GHz; satellite elevation angle = 45°.

The global model has yet to be extensively validated by direct measurements from other regions of the world such as Europe or Asia; however, the results from over a dozen U.S. locations at frequencies from 11 to 30 GHz have shown very good results to date.

Summary of Rain Attenuation Modeling

The models discussed here are only a few of the many developed and proposed for predicting rain-induced path attenuation statistics from rainfall rate measurements near the path. At the present time a single prediction method for worldwide application has not been accepted by the world community.

The CCIR, at its Study Group Meetings in Geneva in June and July 1980, reviewed the advantages and limitations of over two dozen prediction methods and techniques (ref. 43). Its report states,

> With some refinements, it seems that it will be possible to establish a method to predict rain attenuation statistics from point rainfall intensity distributions that will be applicable worldwide. Once this applicability is tested satisfactorily, the sensitivity of the selected method to various input parameters should be evaluated in order to give confidence limits to rain attenuation predictions.

CHAPTER 4

DEPOLARIZATION ON EARTH/SPACE PATHS

A knowledge of the depolarizing characteristics of Earth's atmosphere is important in the design of frequency reuse communications systems employing dual independent orthogonal polarized channels in the same frequency band to increase channel capacity. Frequency reuse techniques, which employ either linear or circular polarized transmissions, can be impaired by the propagation path through a transferral of energy from one polarization state to the other orthogonal state, resulting in interference between the two channels.

This phenomenon, referred to as depolarization or cross polarization, is induced by two sources: hydrometeors, primarily rain or ice crystals, and multipath propagation. (The Faraday effect, which is caused by ionospheric variations of Earth's magnetic field, produces a polarization rotation, not a depolarizing effect, on linear polarized waves only. It may be compensated for rather easily on an Earth/space link and is, therefore, usually not a significant problem).

Multipath-induced depolarization is generally limited to terrestrial links (ref. 44) and can be further induced by the additional effects of the cross-polarized patterns of the receiving antenna (ref. 45).

The major depolarization on Earth/space paths is caused by rain and ice, and recent experimental measurement using satellite beacons from 4 to 30 GHz have greatly increased knowledge of the depolarizing mechanisms and have provided the basis for statistical prediction models.

Radio-wave depolarization is characterized by the presence of an anisotropic propagation medium that produces a different attenuation and phase shift on radio waves with different polarizations. The wave will have its polarization state altered such that power is transferred (or coupled) from the desired polarization state to the undesired orthogonal polarization state, resulting in interference or crosstalk between the two orthogonally polarized channels.

The cross-polarization discrimination, XPD, is defined for linear polarized waves (fig. 15(a)) as

$$\mathrm{XPD} = 20 \log \frac{\mathbf{E}_{11}}{\mathbf{E}_{12}} \tag{37}$$

where $\mathbf{E}_{11}$ is the received electric field in the copolarized (desired) direction and $\mathbf{E}_{12}$ is the electric field converted to the orthogonal cross-polarized (undesired) direction. A closely related measure is the isolation I, which compares the copolarized receiver power with the cross-polarized power received in

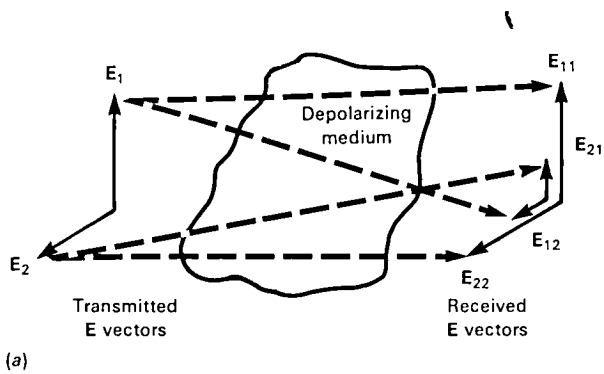

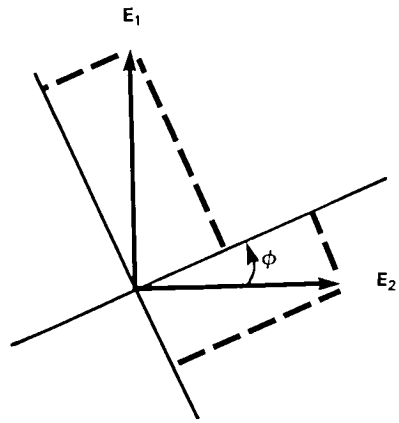

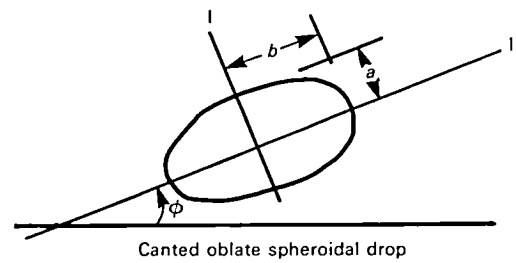

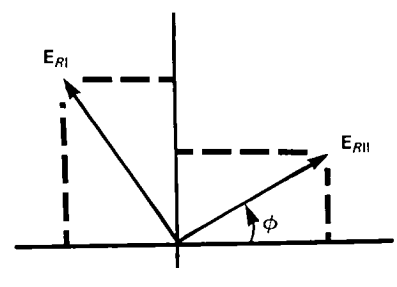

Figure 15.—Vector relationships for a depolarizing medium. (*a*) Copolarized ($\mathbf{E}_{11}$ and $\mathbf{E}_{22}$) and cross-polarized ($\mathbf{E}_{12}$ and $\mathbf{E}_{21}$) waves for linear transmission. (*b*) Classical model for a canted oblate spherical raindrop.

the same polarization state; i.e.,

$$I = 20 \log \frac{\mathbf{E}_{11}}{\mathbf{E}_{21}} \tag{38}$$

(These terms do not have universally accepted definitions. Some authors use the reciprocal of these definitions; or refer to XPD as *I;* or use other terms such as cross-polarization distortion, depolarization ratio, or crosstalk discrimination.)

Isolation takes into account the performance of the receiver antenna, feed, and other components as well as the propagating medium. When the receiver system polarization performance is close to ideal, *I* and XPD are essentially identical, and only the propagating medium contributes depolarizing effects to system performance.

Depolarization Caused by Rain

Rain-induced depolarization is produced from a differential attenuation and phase shift caused by nonspherical raindrops. As the size of raindrops increases, the shape tends to change from spherical drops (which is the preferred shape because of surface tension forces) to oblate spheroids with an increasingly pronounced flat or concave base produced from aerodynamic forces acting upward on the drops. Furthermore, raindrops may also be inclined to the horizontal (canted) because of vertical wind gradients, thus, for linear polarized waves, the depolarization characteristics can depend significantly on the transmitted depolarization angle.

The classical model for a falling raindrop is an oblate spheroid with its major axis canted to the horizontal and with major and minor axes related to the radius of a sphere of equal volume (refs. 46 and 47).

Consider a volume of canted oblate spheroids of extent L in the direction of propagation of two orthogonally polarized linear waves $\mathbf{E}_1$ and $\mathbf{E}_2$ as shown on figure 15(b). The drops are canted at an angle ϕ to the horizontal, with minor and major axes a and b, respectively, in the I and II directions. The transmitted waves can be resolved into components in the I and II directions by

$$\mathbf{E}_{TI} = \mathbf{E}_1 \cos\phi - \mathbf{E}_2 \sin\phi \tag{39a}$$

$$\mathbf{E}_{TII} = \mathbf{E}_1 \sin\phi + \mathbf{E}_2 \cos\phi \tag{39b}$$

The transmission characteristics of the volume of oblate spheroids in the I and II directions are specified by transmission coefficients of the form

$$T_I = \exp\left[-(A_I - i\Phi_I)L\right] \tag{40a}$$

$$T_{II} = \exp\left[-(A_{II} - i\Phi_{II})L\right] \tag{40b}$$

where A_I and A_{II} are the attenuation coefficients and Φ_I and Φ_{II} are the phase shift coefficients in the directions of the minor and major axes (I and II), respectively.

The received waves in the I and II directions are then formed from

$$\mathbf{E}_{RI} = T_I \mathbf{E}_{TI} \tag{41a}$$

$$\mathbf{E}_{RII} = T_{II} \mathbf{E}_{TII} \tag{41b}$$

Combining equations (39), (40), and (41), the resulting received waves in the transmission directions 1 and 2 are

$$\mathbf{E}_{R1} = a_{11}\mathbf{E}_1 + a_{21}\mathbf{E}_2 \tag{42a}$$

$$\mathbf{E}_{R2} = a_{12}\mathbf{E}_1 + a_{22}\mathbf{E}_2 \tag{42b}$$

where a_{11}, a_{12}, a_{21}, and a_{22} are polarization coefficients defined by

$$a_{11} = T_{\mathrm{I}} \cos^2 \phi + T_{\mathrm{II}} \sin^2 \phi \tag{43a}$$

$$a_{22} = T_{\mathrm{I}} \sin^2 \phi + T_{\mathrm{II}} \cos^2 \phi \tag{43b}$$

$$a_{12} = a_{21} = \frac{T_{\mathrm{II}} - T_{\mathrm{I}}}{2} \sin 2\phi \tag{43c}$$

The values of XPD for vertical and horizontal transmissions are then given by

$$\begin{aligned} \mathrm{XPD}_V &= 20 \log \frac{|a_{11}|}{|a_{12}|} \\ &= 20 \log \frac{1 + (T_{\mathrm{II}}/T_{\mathrm{I}}) \tan^2 \phi}{(T_{\mathrm{II}}/T_{\mathrm{I}} - 1) \tan \phi} \end{aligned} \tag{44}$$

$$\begin{aligned} \mathrm{XPD}_H &= 20 \log \frac{|a_{22}|}{|a_{21}|} \\ &= 20 \log \frac{(T_{\mathrm{II}}/T_{\mathrm{I}}) + \tan^2 \phi}{(T_{\mathrm{II}}/T_{\mathrm{I}} - 1) \tan \phi} \end{aligned} \tag{45}$$

Note that both a_{11} and a_{22} are independent of the sign of ϕ. In addition, because $a_{12} = a_{21}$, the cross-polarized components resulting from positive and negative canting angles will cancel each other out.

The XPD for circular transmitted polarization is developed in a similar manner and is expressed in terms of the polarization coefficients as

$$\begin{aligned} \mathrm{XPD}_c &= 20 \log \left(\frac{|a_{11}|}{|a_{12}|}\Big|_{\phi = 45^\circ} |\overline{e^{i2\phi}}| \right) \\ &= 20 \log \left(\frac{T_{\mathrm{II}} + T_{\mathrm{I}}}{T_{\mathrm{II}} - T_{\mathrm{I}}} |\overline{e^{i2\phi}}| \right) \end{aligned} \tag{46}$$

where $\overline{e^{i2\phi}}$ is the mean of $e^{i2\phi}$ taken over the canting angle distribution (ref. 47). Equation (46) holds for either right-hand or left-hand circular polarization.

Measurements on Earth/space paths have tended to confirm that the canting angle tends to be very close to 0° (horizontal) for the majority of nonspherical raindrops (ref. 48). Under these conditions, XPD for circular polarization is identical to XPD for linear horizontal or vertical polarization oriented at 45° from the horizontal.

The complete solution for XPD requires a determination of the transmission coefficients T_{I} and T_{II}. This problem was examined by Oguchi (ref. 46) and solved by employing a spherical expansion solution for a plane wave incident on an oblate spheroid, analogous to the Mie solution for a spherical

drop. An equivolume spherical drop is assumed, which approximates the experimentally observed drop shape by a simple function of the major and minor axes (ref. 49).

Figure 16 presents the differential attenuation ($A_{II} - A_I$) and figure 17 presents the differential phase shift ($\Phi_{II} - \Phi_I$) as functions of frequency for a Laws and Parsons distribution rain at 20° C, with the direction of propagation at 90° to the axis of symmetry of the raindrop (ref. 47). The differential attenuation at 12 GHz, for example, reaches a value of 1.7 dB at a rain rate of 150 mm/hr, while at 30 GHz the differential attenuation is 6 dB for the same rain rate.

Values of XPD for linear horizontal, linear vertical, and circular transmitted waves are shown in figure 18 as functions of copolarized attenuation for five frequencies from 4 to 30 GHz as calculated by Chu for a 100-mm/hr rain rate and a 25° canting angle (ref. 47). For a given copolarized attenuation, XPD decreases (degrades) with decreasing frequency. Communications systems at 4 and 6 GHz, however, seldom experience rain attenuation of more than a few decibels. The value of XPD for vertical polarized transmission is generally greater (better) than for horizontal polarized transmission at the same attenuation level, except at 4 GHz, where the differential phase shift dominates the depolarization effect. Circularly polarized waves produce values of XPD about 10 dB lower (worse) than horizontally polarized waves at the same attenuation level.

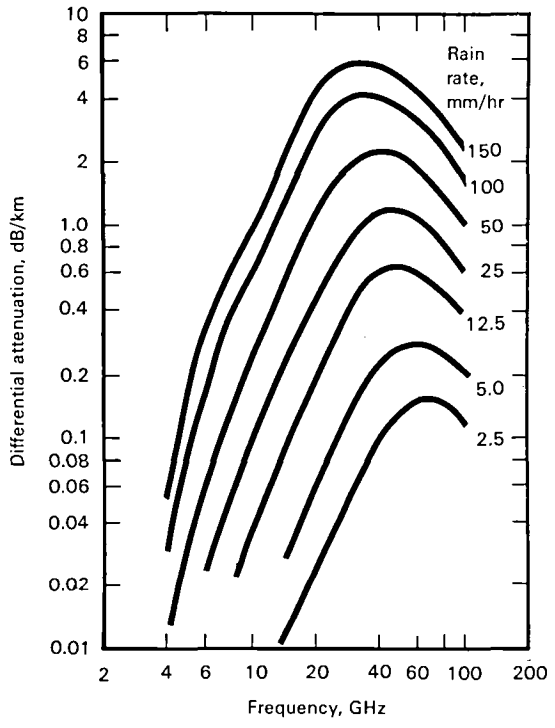

Figure 16.—Differential attenuation as a function of frequency and rain rates specified in millimeters per hour.

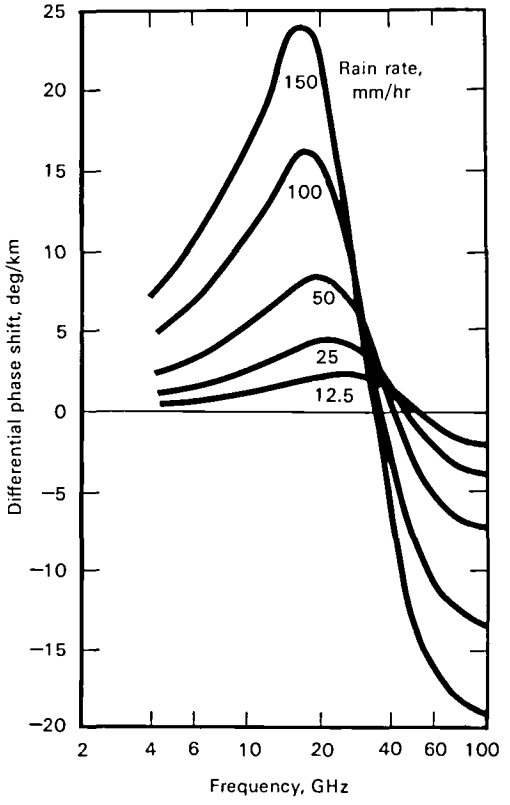

Figure 17.—Differential phase shift as a function of frequency and rain rates specified in millimeters per hour.

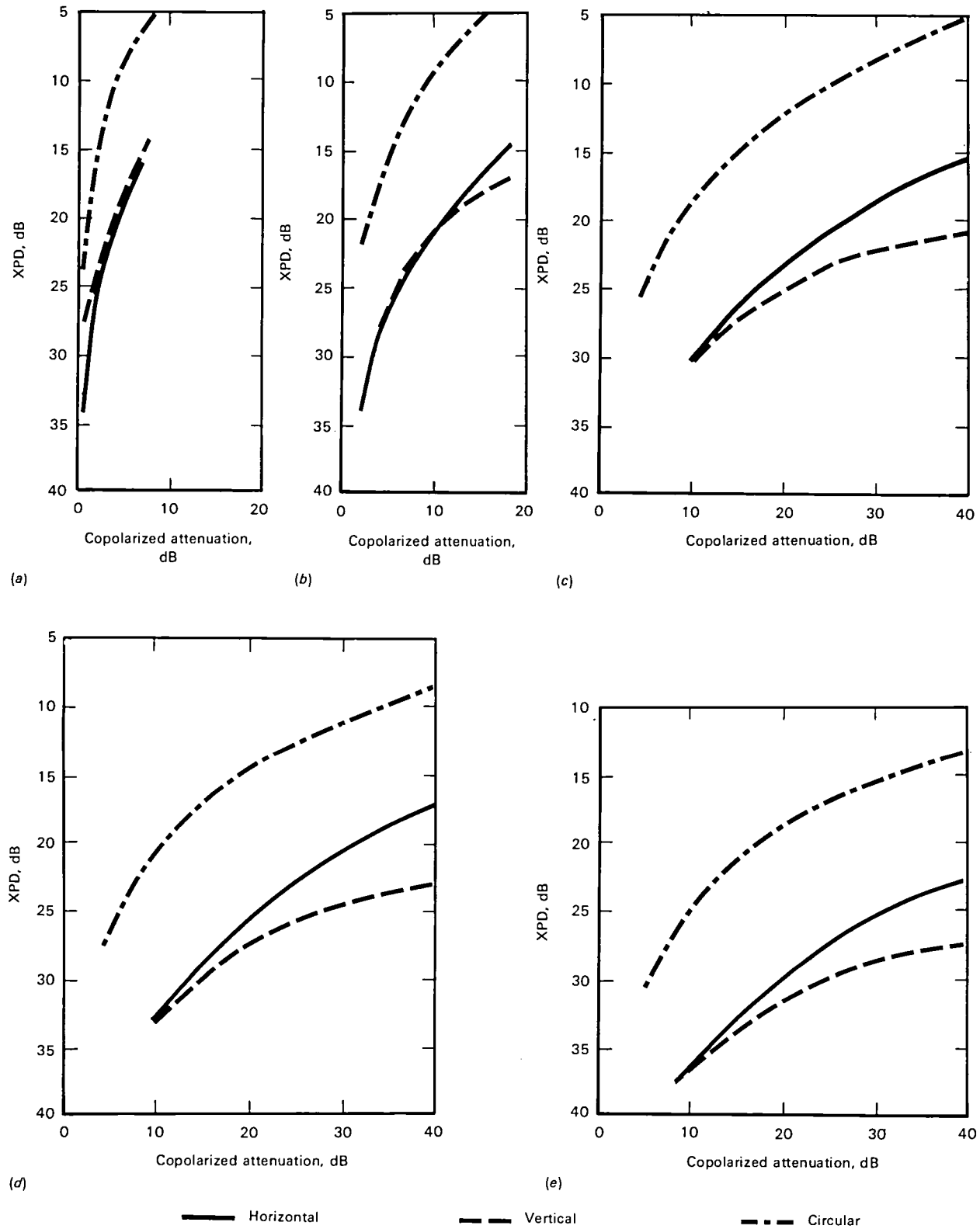

Figure 18.—Cross-polarization discrimination for linear horizontal, linear vertical, and circular transmitted waves at 100 mm/hr. (*a*) 4 GHz. (*b*) 6 GHz. (*c*) 11 GHz. (*d*) 18 GHz. (*e*) 30 GHz.

Depolarization and Rain Attenuation

An empirical relationship of the form

$$\text{XPD} \cong U - V \log A \tag{47}$$

has been observed between the measured statistics of rain-induced XPD and copolarized attenuation A for both terrestrial and Earth/space paths. The values of U and V are empirically determined constants that depend on frequency, polarization, elevation angle, canting angle, and other link parameters.

A theoretical basis for the relationship between rain depolarization and attenuation given in equation (47) was developed by Nowland et al. from small argument approximations applied to the scattering theory of Oguchi for an oblate spheroidal raindrop (ref. 50). The constants U and V were found to be approximated by

$$U \cong 20 \log \frac{\exp(-2\sigma_\phi^2)|A_{\text{II}} - A_{\text{I}}| \cos^2\theta \sin(2|\phi - \delta|)}{2} \tag{48}$$

$$V \cong 20 \tag{49}$$

where θ is the elevation angle, σ_ϕ is the standard deviation for the canting angle distribution, and δ is the incident wave polarization tilt angle with respect to the local horizontal. For circular polarization $|\phi - \delta| = 45°$.

A general prediction equation for XPD from copolarized attenuation has yet to be fully established; however, the CCIR, at its Study Groups Interim Meetings in Geneva in June and July 1980, recommended the following semiempirical expression for the constant U:

$$U = 30 \log f - 40 \log(\cos\theta) - 20 \log(\sin 2|\phi - \delta|) \qquad \text{dB} \tag{50}$$

where f is the frequency in gigahertz; θ, ϕ, and δ are, respectively, the elevation angle, canting angle, and polarization tilt angle, all in degrees (ref. 51). The value of V is set equal to 20.

Semiempirical prediction techniques that employ relations between XPD and point rain rate have also been proposed, but they have yet to be extensively evaluated or validated with reliable measured data.

Depolarization Measurements

The direct measurement of depolarization effects on Earth/space paths began with the ATS 6 beacons in 1975 and has continued through the present with the CTS, COMSTAR, and SIRIO satellites discussed in reference 16. The largest data base of depolarization measurements has been acquired at Blacksburg, Va., by the Virginia Polytechnic Institute and State University (VPI and SU). Figure 19(*a*) shows a plot of 11.7-GHz isolation versus attenuation obtained for calendar year 1978 with the CTS satellite at an elevation angle of 33°. Three curves are superimposed on the data points. The instantaneous fit curve is a least-squares fit of the isolation-attenuation points for all attenuation values

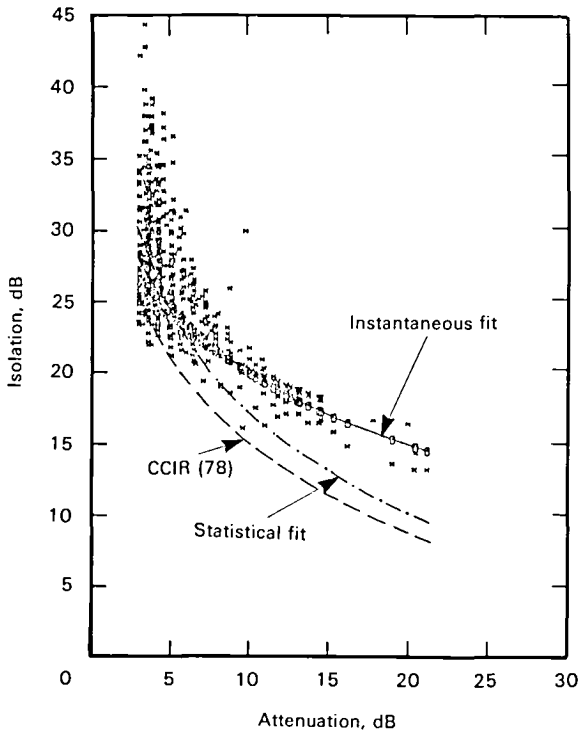

(a)

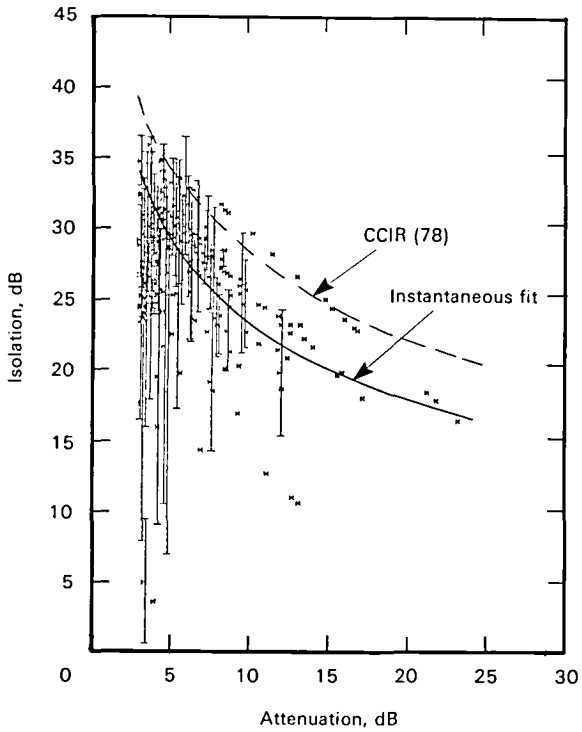

(b)

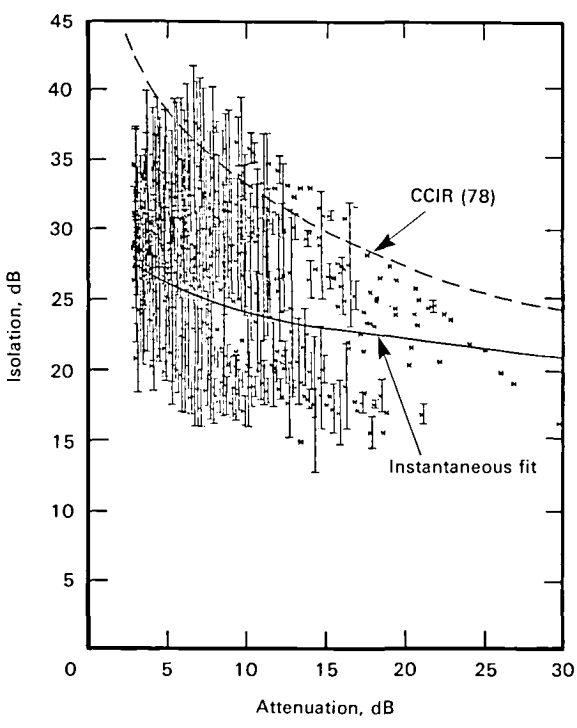

(c)

Figure 19.—Isolation measurements for calendar year 1978 at Blacksburg, Va. (*a*) CTS satellite; 11.7 GHz; elevation angle = 33°. Instantaneous fit: $I = 36.3 - 16.2 \log A$; $5 < A < 30$ dB. CCIR (78): $I = 35.1 - 20 \log A$. Statistical fit: $I = 41 - 23.2 \log A$. (*b*) COMSTAR; 19.04 GHz; elevation angle = 46°. Instantaneous fit: $I = 43.9 - 19.6 \log A$; $r^2 = 0.34$. CCIR (78): $I = 48.6 - 20 \log A$. (*c*) COMSTAR; 28.56 GHz; elevation angle = 46°. Instantaneous fit: $I = 31.2 - 7 \log A$. CCIR (78): $I = 53.8 - 20 \log A$.

greater than 5 dB. The statistical fit curve is based on a comparison of equal probability isolation and attenuation from the annual cumulative distributions. The CCIR (78) curve is based on the CCIR prediction given by equation (50). The data are seen to agree fairly well with the expected trend: however, the CCIR prediction curve tends to overpredict the isolation effects for a given attenuation value.

Similar displays for 19.04- and 28.56-GHz isolation measurements taken with COMSTAR are shown in figures 19(*b*) and 19(*c*). The spread of data points increases with increasing frequency, and the CCIR curves tend to underpredict the isolation by 5 dB or more at both frequencies.

The cumulative distribution of XPD is a useful parameter in the determination of the effects of depolarization because it allows a determination of the extent of the problem to be encountered on an operational link. Figure 20 presents the cumulative distributions of 11.7- and 28.56-GHz XPD as measured at Blacksburg, Va., for the years 1977, 1978, 1979 (ref. 52). The solid curves present the measured distributions and the dashed curves are the distributions as scaled from the attenuation

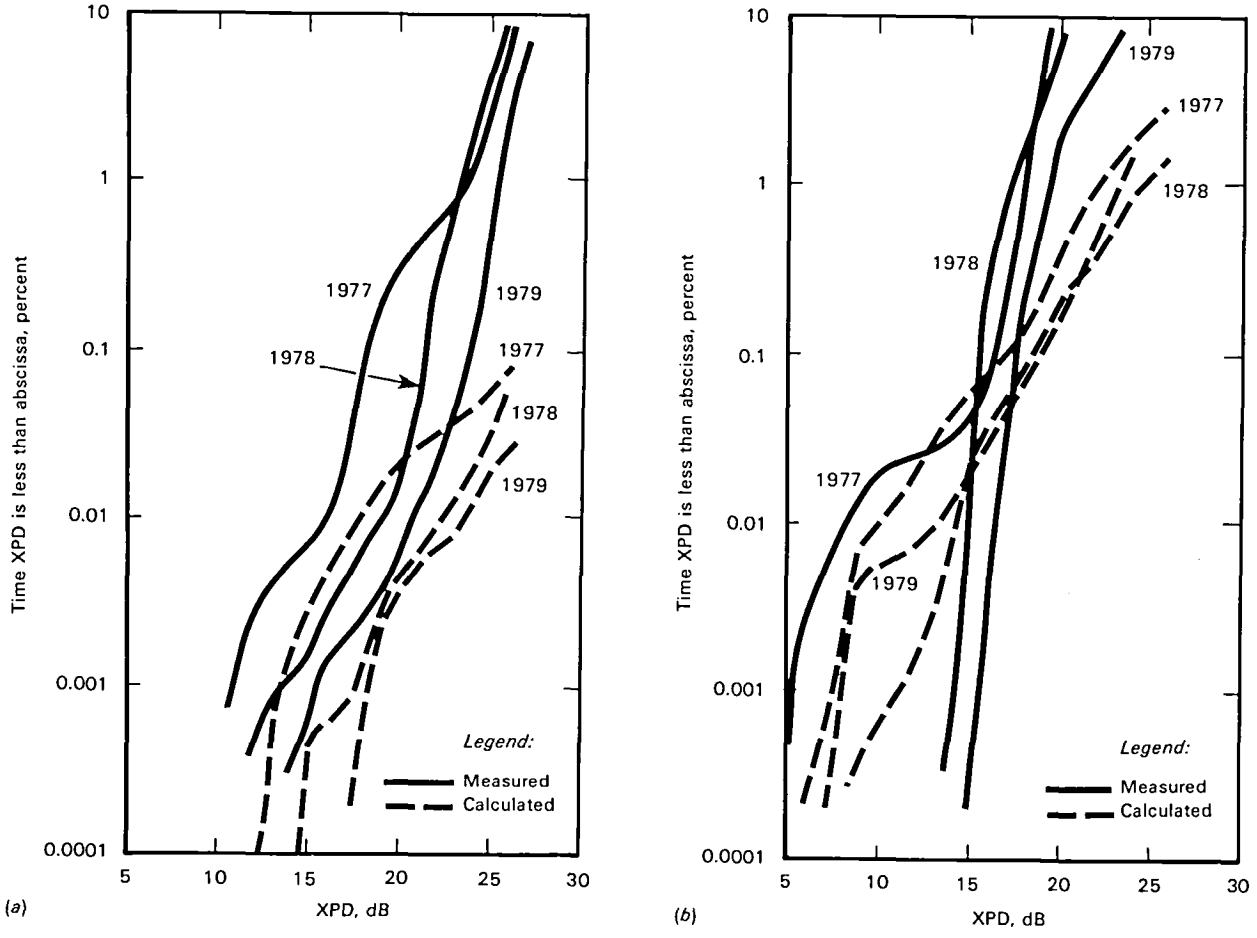

Figure 20.—XPD distributions for the years 1977, 1978, and 1979 measured at Blacksburg, Va. (*a*) 11.7 GHz; elevation angle = 33°; right-hand circular polarization. (*b*) 28.56 GHz; elevation angle = 46°; $\delta = 60°$; linear polarization.

measurements, using the instantaneous fit equations

$$I = 41 - 23.2 \log A \tag{51a}$$

$$I = 36.5 - 16.65 \log A \tag{51b}$$

for 11.7 and 28 GHz, respectively.

Table 10 presents a summary of long-term depolarization statistics measured on satellite beacons at frequencies of 4, 11.7, 19, and 28 GHz. The columns labeled XPD present the cross polarization discrimination for the given percent of the total observation period. The transmit polarization tilt angle is referenced to the local horizontal. The measurements indicate that a 20-dB XPD can be maintained for 99.99 percent of the time for frequencies of 4 or 11.7 GHz, but the reliability drops to 99.95 percent at 19 or 28 GHz. The measurements at 4 and 11.7 GHz were for right-hand circular polarization, while for 19 and 28 GHz were for linear polarization at the tilt angle listed.

A satellite communications system employing frequency reuse will undergo a system outage when attenuation or depolarization design levels are exceeded, thus it is necessary to consider both attenuation and depolarization distributions when determining system performance criteria. A useful method of displaying both attenuation and depolarization statistics on a single plot was developed by Arnold et al. for the measured data from Holmdel (ref. 49). Figure 21 shows the 19-GHz linear polarized attenuation and depolarization data displayed as a combined distribution. The time $T(A, D)$ on the ordinate for each point on the curves represents the sum of two terms:

$$T(A, D) = \sum_{\substack{\alpha > A \\ \text{all } \delta}} t(\alpha, \delta) + \sum_{\substack{\alpha < A \\ \delta > D}} t(\alpha, \delta) \tag{52}$$

where attenuation α exceeds the value A or depolarization (XPD) δ exceeds the value D. Values of A are on the abscissa, and values of D are given to the right of the curves. The first term in equation (52) contains all the time for which the attenuation exceeds the value A, and the second term contains the additional time for which XPD exceeds the value D even though the attenuation is less than A. The bottom curve represents the cumulative distribution due to attenuation only.

As an example of the application of this plot, consider the case of a link with a 10-dB maximum attenuation requirement. The bottom curve indicates that attenuation exceeded 10 dB for 262 min (0.05 percent) of the year. Under the same attenuation conditions, a dual polarized link with a 20-dB XPD requirement would experience a 273-min (0.052 percent) outage, a small increase over that for attenuation alone. A link that could only tolerate a 25-dB XPD would experience a 578-min (0.11 percent) outage at the 10-dB attenuation level, which is more than twice the outage time from attenuation considerations alone.

The flattening of the distributions for attenuation values greater than 15 to 20 dB indicates that system margins in exceess of 20 dB will not significantly decrease outage time on a dual polarization system.

TABLE 10.—SUMMARY OF CROSS POLARIZATION DISCRIMINATION MEASUREMENTS

Location	Transmit polarization (tilt angle, deg)	Frequency, GHz	Elevation angle, deg	Observation time period	XPD, dB, for given percent time							Reference
					1	0.5	0.1	0.05	0.01	0.005	0.001	
Taipei, Taiwan	RHC	4	20	—	<35.0	31.0	22.0	20.5	18.0	17.5	16.0	53
Lario, Italy	RHC	4	25	Mar. 1977 to June 1978	41.0	37.0	30.5	28.0	24.0	22.0	20.0	53
Ibaraki, Japan	RHC	4	30	—	<35.0	32.0	30.5	28.0	24.0	22.0	20.0	53
Blacksburg, Va.	RHC	11.7	33	Jan. to Dec. 1978	24.0	23.5	22.0	21.5	20.0	18.0	14.0	52
				Jan. to Dec. 1979	26.0	25.5	24.5	24.0	21.0	20.0	16.0	
Austin, Tex.	RHC	11.7	49	June 1976 to June 1979	<35.0	34.0	28.0	25.5	20.5	18.0	15.0	54
Holmdel, N.J.	21° HL	19	38.6	May 1977 to May 1978	—	30.0	24.0	22.0	16.0	11.0	>10.0	48
	78° VL	19	38.6	May 1977 to May 1978	—	30.0	25.0	23.0	18.0	15.0	>10.0	
Holmdel, N.J.	78° VL	28	38.6	May 1977 to May 1978	—	28.0	22.0	20.5	12.0	>10.0	—	48
Blacksburg, Va.	60° VL	28	46	Jan to Dec. 1978	18.0	17.0	15.0	14.0	13.0	12.5	9.5	52
				Jan. to June 1979	20.0	19.0	18.0	17.0	12.5	9.0	7.0	

HL = horizontal linear; VL = vertical linear; RHC = right-hand circular.

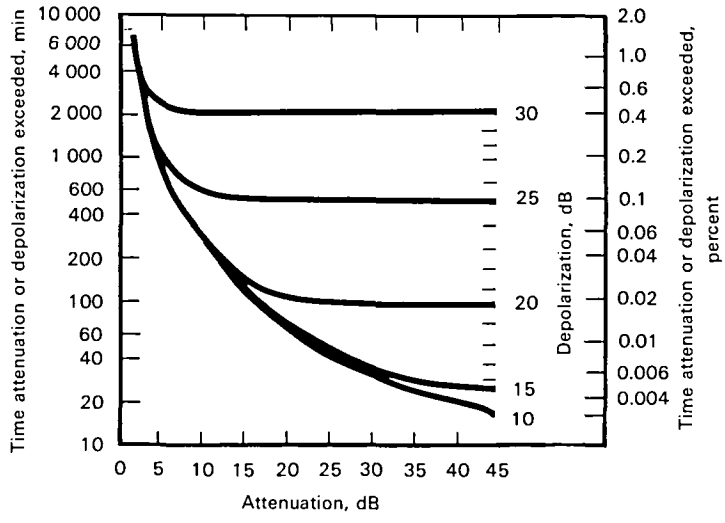

Figure 21.—19-GHz linear polarized attenuation and depolarization distributions for Crawford Hill, Holmdel, N.J.; May 18, 1977, to May 18, 1978; elevation angle = 38.6°; polarization: 21° from vertical.

Ice Crystal Depolarization

Depolarization caused by ice crystals above the melting layer has been observed on Earth/space paths from measurements using satellite beacons. This effect, initially referred to as "anomalous" depolarization because its cause was unknown, is characterized by a strong depolarization accompanied by very low copolarized attenuation. Also, abrupt changes in XPD have been observed to coincide with lightning discharges in the area of the slant path, suggesting a change in the alignment of the ice crystals.

The frequency of occurrence and severity of ice crystal depolarization appear to vary with climate and geography. Measured effects have been observed in both the United States and in Europe at frequencies from 11 to 30 GHz.

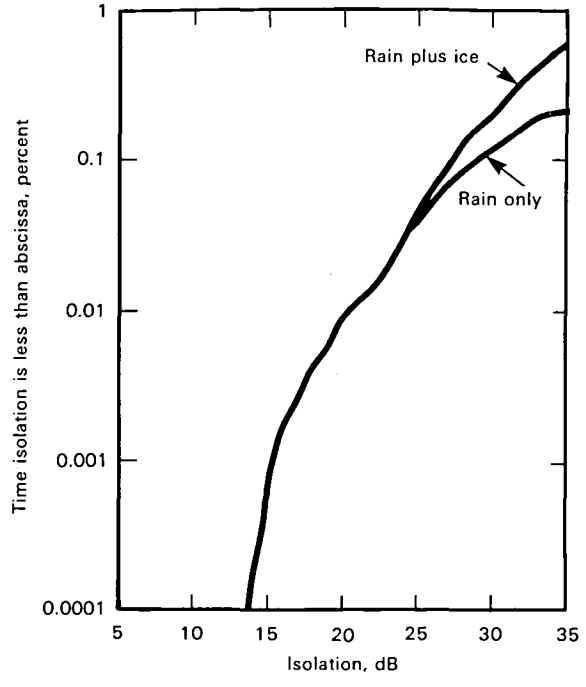

Figure 22.—Rain ($A > 1$ dB) and ice depolarization distributions measured at Austin, Tex. June 1976 to June 1979; 11.7 GHz; elevation angle = 49°; right-hand circular polarization.

Ice depolarization was observed in early depolarization measurements using the linearly polarized 20-GHz ATS 6 beacon, but it was not identified as a significant effect until the ATS 6 measurements were made in Europe a year later and the CTS and COMSTAR measurements were made in the United States (ref. 55).

Ice crystals produce a nearly pure differential phase shift without any accompanying differential attenuation, which explains the depolarization effects observed in the absence of copolarized attenuation.

The relative occurrence of ice depolarization versus rain depolarization can be observed in figure 22, which shows the 3-year cumulative distributions of isolation measured at Austin, Tex., at 11.7 GHz (ref. 54). The curve labeled "Rain plus ice" is for all the observed depolarization, while the "rain only" curve corresponds to those measurements in which the attenuation was greater than 1 dB. The ice contribution appears significant only for isolation values greater than 25 dB where ice effects are present about 10 percent of the time. The ice effects exceed 50 percent of the time at the 35-dB isolation value, resulting in an increase in the distribution from 0.2 to 0.54 percent.

CHAPTER 5

SKY NOISE

The gaseous constituents of Earth's atmosphere, and clouds or precipitation when present, all act as an absorbing medium to electromagnetic waves; therefore, they are also sources of thermal noise power radiation. This radiation, often called sky noise, is particularly significant on Earth/space paths with low-noise receiver systems because the radiation contributes directly to system noise temperatures of both the uplink and downlink receivers.

The effective sky noise temperature T_s in a given direction is determined from radiative transfer considerations by the equation

$$T_s = \int_0^\infty T(s)\gamma(s) \exp\left[-\int_0^s \gamma(s')ds'\right] ds \tag{53}$$

where $T(s)$ is the temperature of the medium in degrees kelvin, $\gamma(s)$ is the absorption coefficient of the medium in reciprocal kilometers, and s is the distance along the path from the antenna in kilometers. If $T(s)$ is replaced by a mean path temperature T_m, equation (53) simplifies to

$$T_s = T_m\left(1 - \frac{1}{L}\right) \tag{54}$$

where L is the loss factor resulting from the absorbing medium.

If a horizontally stratified atmosphere is assumed, T_s at an elevation angle θ is given by

$$T_s(\theta) = T_m(1 + L_0^{-\text{cosec}\,\theta}) \qquad \theta > 15° \tag{55}$$

where L_0 is the loss factor in the zenith ($\theta = 90°$) direction.

Emission from Atmospheric Gases

The sky noise caused by the atmospheric gases for an infinitely narrow beam at various elevation angles and for frequencies between 1 and 100 GHz is shown in figure 23 (ref. 56). The curves are for a surface temperature of 20° C; surface pressure of 1 atm; and a surface water vapor concentration of 10 g/m^3, corresponding to a relative humidity of 58 percent. At $\theta = 10°$ the results give sky temperatures of 22, 100, and 63 K for 12, 20, and 30 GHz, respectively. Sky temperature contributions caused by gaseous constituents can be significant for extremely low noise receiver systems, where system noise temperatures below 300 K are required.

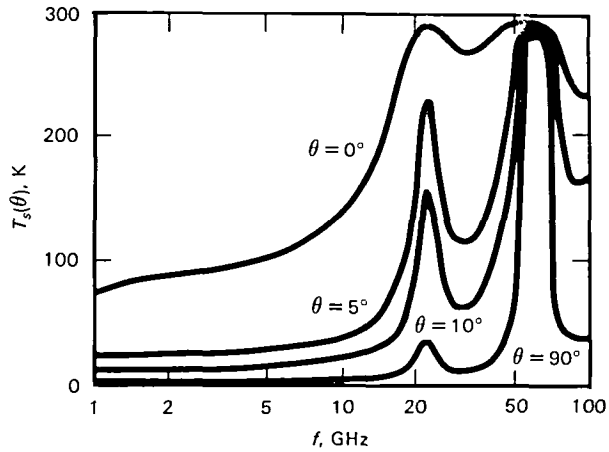

Figure 23.—Sky noise resulting from atmospheric gases as a function of frequency and elevation angle. Surface temperature = 20° C; Pressure = 1 atm; water vapor concentration = 10 g/m^3.

Emission Caused by Clouds and Precipitation

The sky noise resulting from absorption in clouds and precipitation can also be determined from equations (53) to (55) by reexpressing the loss factor in terms of the attenuation coefficient:

$$T_s = T_m(1 - 10^{-A/10}) \tag{56}$$

where A is the path attenuation in decibels. Values for T_m have been calculated from satellite beacon and radiometer measurements to be approximately 270 K. The increase in receiver system noise caused by the increased sky noise from a rain fade is listed in table 11 for systems with system noise figures from 2 to 10 dB. The rain is seen to degrade the 2- and 3-dB systems significantly at all fade levels, producing effective noise figures of 4.01 and 4.67 dB, respectively, at a 30-dB fade level. This increase in system noise adds directly to the signal loss produced by the rain attenuation in the determination of system carrier to noise ratio. For example, consider the system with a 2-dB noise figure experiencing a 15-dB rain fade. The total reduction in system carrier-to-noise ratio would be 15 + 1.96 or nearly 17 dB below that for clear sky conditions.

TABLE 11.—INCREASE IN RECEIVER SYSTEM NOISE CAUSED BY NOISE CONTRIBUTION FROM A RAIN FADE

Rain fade level, dB	Sky noise contribution caused by rain, K	"Effective" noise, dB, for given system noise specified in decibels				
		2 (170 K)	3 (290 K)	4 (438 K)	6 (865 K)	10 (2610 K)
1	56	2.50	3.41	4.32	6.21	10.08
3	135	3.12	3.92	4.74	6.48	10.20
5	185	3.47	4.21	4.98	6.65	10.27
10	243	3.85	4.53	5.25	6.83	10.35
15	261	3.96	4.62	5.33	6.89	10.37
20	267	3.99	4.65	5.35	6.91	10.38
30	270	4.01	4.67	5.37	6.91	10.39

CHAPTER 6

SCINTILLATION AND BANDWIDTH EFFECTS

Scintillation on a radio-wave path describes the phenomenon of rapid fluctuations of the amplitude, phase, or angle of arrival of the wave passing through a medium with small-scale refractive index irregularities that cause changes in the transmission path with time. Scintillation effects, often referred to as atmospheric multipath fading, can be produced in both the troposphere and the ionosphere, with the major ionospheric effects occurring at frequencies below 1 to 2 GHz. To a first approximation, the refractive index structure can be considered to be horizontally stratified, and variations appear as thin layers that change with altitude. Slant paths at low elevation angles (i.e., highly oblique to the layer structure) tend to be affected most significantly by scintillation conditions.

Tropospheric scintillation is typically produced in the first few kilometers of altitude by high humidity gradients and temperature inversion layers. The effects are seasonally dependent, and vary from day-to-day, as well as with the local climate.

Ionospheric scintillation is produced near the altitude of maximum electron density, the *F* region, at heights of approximately 200 to 400 km. The conditions for scintillation are most prevalent in the equatorial regions, at high latitude locations, and during periods of high sunspot activity.

Amplitude Scintillations on Earth/Space Paths

Amplitude scintillations have been observed in northwest Europe and in North America on several satellite paths and frequencies ranging up to above 30 GHz. Several organizations reported results using the ATS 6 satellite at frequencies of 2, 20, and 30 GHz and other satellite transmissions at 4, 6, and 7 GHz (ref. 57). There is broad agreement at all frequencies showing scintillations at high elevation angles (20° to 30°) in a temperate climate on the order of 1 dB (peak to peak) in clear sky in summer, 0.2 to 0.3 dB in winter, and 2 to 6 dB in some types of cloud. Data on the rate of fading are inconclusive; fluctuations from 0.5 Hz to over 10 Hz have been observed. A much slower fading component, with a period of 1 to 3 min, has occasionally been observed along with the more rapid fluctuations.

The measurements show a very definite increase in the magnitude of scintillation effects as the elevation angle is reduced below 10°. Deep fades of 20 dB or more with a few seconds' duration have been observed; such fades are indicative of a multipath mechanism.

Figure 24 shows an example of amplitude scintillation measurements at 2 and 30 GHz made by ATS 6 at Columbus, Ohio, at elevation angles of 4.95° and 0.38° (ref. 58). Measurements of this type were made in clear weather conditions up to elevation angles of 44°, and the data are summarized in

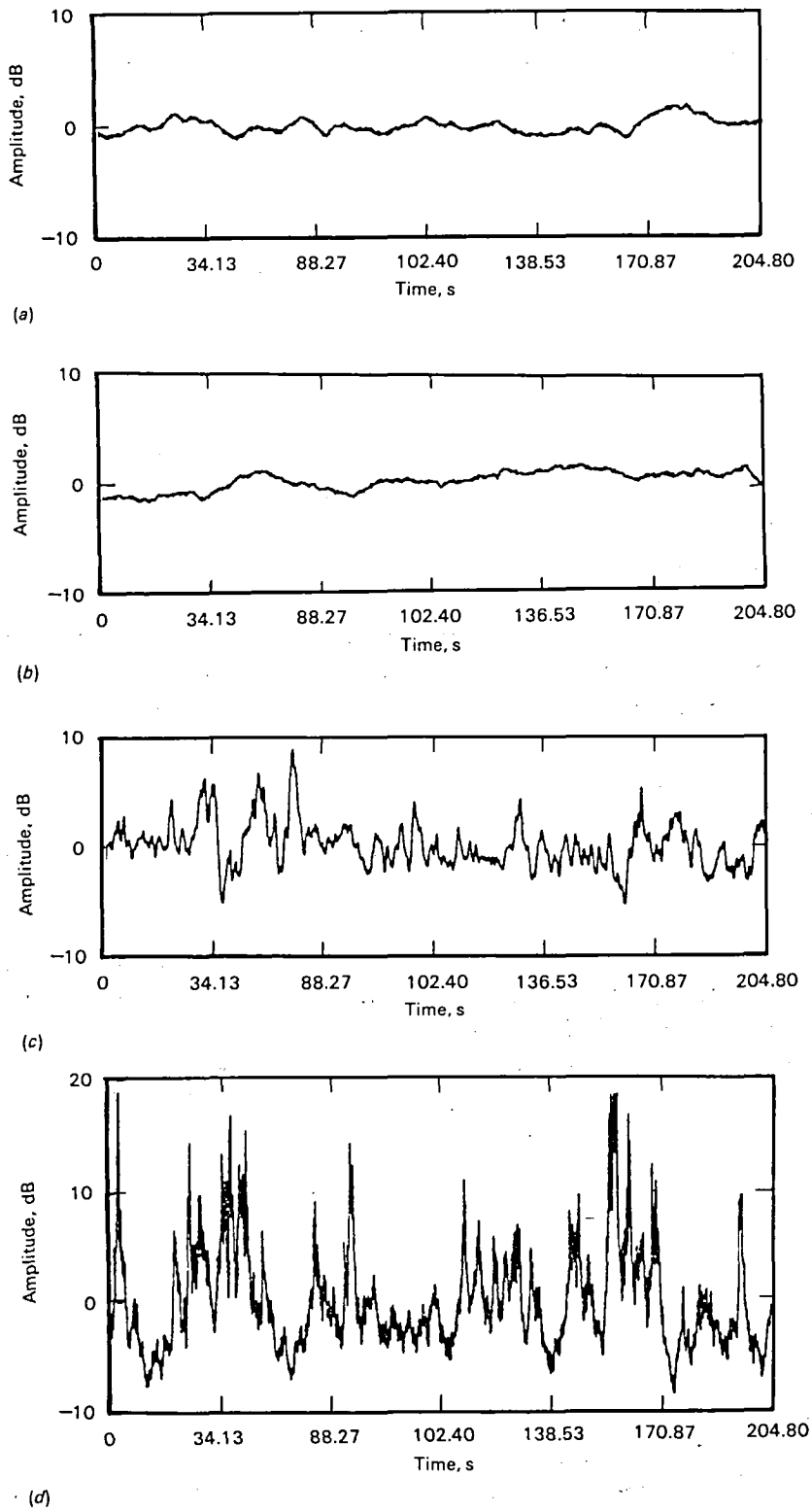

Figure 24.—Amplitude scintillation measurements made by ATS 6 at Columbus, Ohio. (*a*) 2-GHz receiver; elevation angle = 4.95°. (*b*) 2-GHz receiver; elevation angle = 0.38°. (*c*) 30-GHz receiver; elevation angle = 4.95°. (*d*) 30-GHz receiver; elevation angle = 0.38°.

figure 25, in which the mean amplitude variance is plotted for 2 and 30 GHz as a function of elevation angle. The curves on the figure represent minimum mean square error fits to the assumed cosecant power law relationship

$$\sigma^2 = A(\text{cosec } \theta)^B \tag{57}$$

where θ is the elevation angle. The resulting B coefficients compare well, within their range of error, with the expected theoretical value, $B = 1.833$ for a Kolmogorov type turbulent atmosphere.

Antenna Gain Degradation

The antenna gain in a communications system is generally defined in terms of the behavior of the antenna when illuminated by a uniform plane wave. Amplitude and phase fluctuations induced by the atmosphere can produce perturbations across the physical antenna aperture resulting in a reduction of total power available at the feed. The resulting effect on the antenna will look to the system like a loss of antenna gain, or a gain degradation. This loss may be interpreted in two ways: (1) in terms of angle of arrival fluctuations that cause the incident signal to arrive from directions other than the maximum gain direction or (2) as a phase dispersion of the ray paths that reflect from the surface of the antenna reflector, resulting in a summation at the feed point of rays no longer in phase.

Gain degradation will increase as the electrical receiving aperture size increases, hence the problem will become more significant as operating frequency and/or physical aperture size increases. Also, the effect will be more pronounced as the path length in the atmosphere increases; e.g., for low-elevation-angle Earth/space links.

Estimates of gain degradation have been determined by application of conventional atmospheric turbulence theory to an Earth/space path (ref. 59). Figure 26 presents gain degradation as a function of elevation angle at a frequency of 30 GHz for antenna beamwidths from 0.3° to 0.05°. Gain degradation is less than 2 dB for elevation angles above 10°, even for 0.05° beamwidth. These curves represent gain degradation caused by atmospheric turbulence only; additional effects could be expected from atmospheric gases and clouds in the beam.

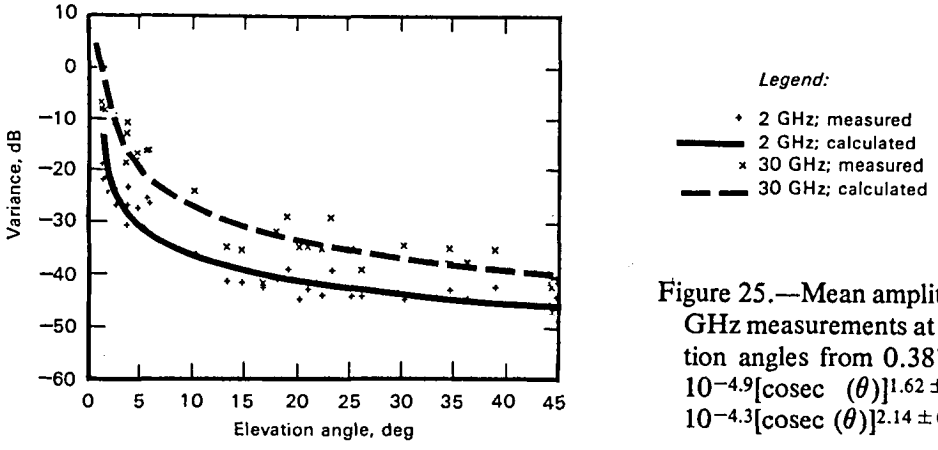

Figure 25.—Mean amplitude variance for 2- and 30-GHz measurements at Columbus, Ohio, for elevation angles from 0.38° to 44°. At 2 GHz: $\sigma^2 = 10^{-4.9}[\text{cosec } (\theta)]^{1.62 \pm 0.2}$. At 30 GHz: $\sigma^2 = 10^{-4.3}[\text{cosec } (\theta)]^{2.14 \pm 0.3}$.

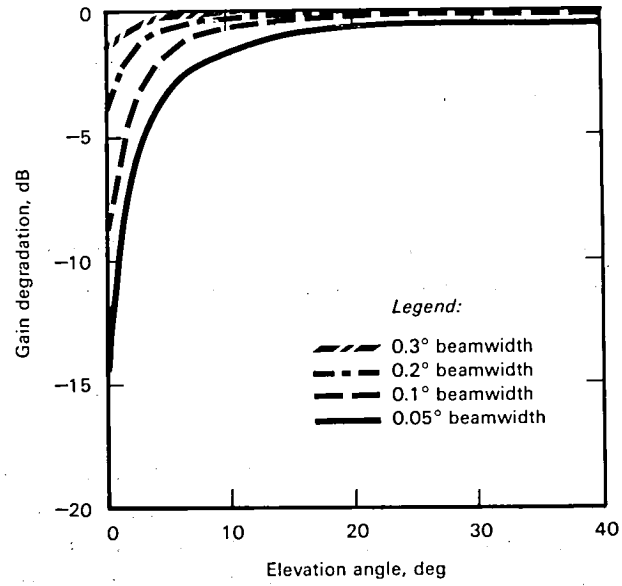

Figure 26.—Antenna gain degradation at 30 GHz as a function of elevation angle for antenna beamwidths of 0.3°, 0.2°, 0.1°, and 0.05°.

For most practical Earth/space communications links, which operate at elevation angles well above 10°, gain degradation induced by atmospheric turbulence is not expected to degrade the link to any significant level.

Bandwidth Coherence

Most of the propagation results discussed to this point involve Earth/space transmissions at a single frequency. The question of whether Earth's atmosphere will produce a limitation on the bandwidth of transmissions on an Earth/space link is particularly important as the next generation of satellite systems moves to wider bandwidths and digital techniques involving large numbers of carriers spread out over large channel bandwidths.

Theoretical estimates of the effects of rain on wideband transmissions have indicated that the atmosphere can support a bandwidth of several gigahertz at carrier frequencies above 10 GHz, at which point the bulk attenuation effects will predominate over any bandwidth reduction effect such as frequency selective fading or severe amplitude and/or phase dispersion (refs. 60 and 61).

Experimental verification of bandwidth coherency on an Earth/space path was first accomplished at 20 and 30 GHz with the ATS 6 satellite (ref. 62). Nine sidebands spread out over a 1.44-GHz bandwidth were used to determine the frequency/phase characteristics of the atmosphere during rain. The results showed no measurable selective fading over the 1.44-GHz bandwidth, even for severe rain fades. Amplitude and phase fluctuations were within the measurement accuracy of the receiving equipment; i.e. ±0.5 dB and 4°, respectively.

Similar results were reported recently on measurements with the COMSTAR satellite beacons (ref. 63). In the experiment amplitude and phase dispersion over a 528-MHz bandwidth at 28 GHz

were measured for a 1-yr period, and no evidence of any amplitude or phase dispersion other than the frequency dependence caused by the bulk properties of water in rain was observed. Cox et al. conclude "amplitude and phase dispersion should not pose a problem for wideband (on the order of 1 GHz) Earth/space communciations systems operating at frequencies greater than 10 GHz with relatively large elevation angles (>15°) from the Earth terminals."

Office of Space and Terrestrial Applications
National Aeronautics and Space Administration
Washington, D.C. 20546

REFERENCES

1. Morgan, W. L.: "Satellite Utilization of the Geostationary Orbit." *COMSAT Tech. Rev.,* vol. 6, no. 1, Spring 1976, pp. 195-205.

2. Morgan, W. L.: "Geosynchronous Satellite Log." *COMSAT Tech. Rev.,* vol. 8, no. 1, Spring 1978, pp. 219-237.

3. Van Vleck, J. H.; and Weisskopf, V. F.: "On the Shape of Collision Broadened Lines." *Rev. Mod. Phys.,* vol. 17, 1945, pp. 227-236.

4. "Attenuation by Atmospheric Gases." *Recommendations and Reports to the CCIR,* vol. 5, rept. 719, International Telecommunications Union (Geneva), 1978, pp. 97-102.

5. Crane, R. K.; and Blood, D. W.: *Handbook for the Estimation of Microwave Propagation Effects-Link Calculations for Earth-Space Paths.* Document No. P-7376-TR1, Environmental Research and Technology Inc. (prepared for NASA Goddard Space Flight Center under Contract NASS-25341), June 1979.

6. Goldhirsh, Julius; and Katz, I.: "Useful Experimental Results for Earth-Satellite Rain Attenuation Modeling." *IEEE Trans. Antennas Propagat.,* vol. AP-27, no. 3, May 1979, pp. 413-415.

7. Van De Hulst, H. C.: *Light Scattering by Small Particles.* John Wiley & Sons, Inc., 1957.

8. Laws, J. O.; and Parsons, D. A.: "The Relation of Raindrop-Size to Intensity." *Trans. Amer. Geophys. Union,* vol. 24, 1943, pp. 452-460.

9. Marshall, J. S.; and Palmer, W. McK.: "The Distribution of Raindrops With Size." *J. Meteorol.,* vol. 5, Aug. 1948, pp. 165-166.

10. Joss, J.; Thams, J. C.; and Waldvogel, A.: "The Variation of Raindrop Size Distributions at Locarno." *Proc. Int. Conf. Cloud Phys.* (Toronto, Canada), 1968, pp. 369-373.

11. Ryde, J. W.; and Ryde, D.: *Attenuation of Centimetre and Millimetre Waves by Rain, Hail, Fogs, and Clouds.* Rept. No. 8670, Research Laboratories of the General Electric Co. (Wembley, England), 1945.

12. Gunn, K. L. S.; and East, T. W. R.: "The Microwave Properties of Precipitation Particles." *Quart. J. Roy. Meteorol. Soc.,* vol. 80, 1954, pp. 522-545.

13. Olsen, R. L.; Rogers, D. V.; and Hodge, D. B.: "The aR^b Relation in the Calculation of Rain Attenuation." IEEE Trans. Antennas Propagat., vol. AP-26, no. 2, Mar. 1978, pp. 318-329.

14. Medhurst, R. G.: "Rainfall Attenuation of Centimeter Waves: Comparison of Theory and Measurements." *IEEE Trans. Antennas Propagat.,* vol. AP-13, July 1965, pp. 550-564.

15. Setzer, D. E.: "Computed Transmission Through Rain at Microwave and Visible Frequencies." *Bell Syst. Tech. J.*, vol. 49, Oct. 1970, pp. 1878-1892.

16. Kaul, R.; Rogers, D.; and Bremer, J.: *A Compendium of Millimeter Wave Propagation Studies Performed by NASA.* ORI TR 1278, ORI, Inc., Nov. 1977.

17. Kaul, R.; Wallace, R.; and Kinal, G.: *A Propagation Effects Handbook for Satellite Systems Design.* ORI TR 1679, NASA Headquarters, Mar. 1980.

18. Ippolito, L. J.: *11.7 GHz Attenuation and Rain Rate Measurements With the Communications Technology Satellite (CTS).* NASA TM 80283, Apr. 1979.

19. Nackoney, O. G.: *CTS 11.7 GHz Propagation Measurements.* Third Year's Data and Final Report, TR 79-471.3, GTE Laboratories Inc. (Waltham, Mass.), Oct. 1979.

20. Arnold, H. W.; Cox, D. C.; and Rustako, A. J., Jr.: "Rain Attenuation at 10-30 GHz Along Earth-Space Paths: Elevation Angle, Frequency, Seasonal and Diurnal Effects." *ICC '80 Conference Record* (Seattle, Wash.), June 9-12, 1980.

21. Bostian, C. W.; Stutzman, W. L.; Manus, E. A.; Wiley, P. H.; Marshall, R. E.; and Santago, P.: "Summary of 1978 Attenuation and Depolarization Measurements Made With the CTS (11.7 GHz) and COMSTAR (19.04 and 28.56 GHz) Beacons." Paper presented at the 1979 IEEE URSI Int. Symp. (Seattle, Wash.), June 20, 1979.

22. Vogel, W. J.: *CTS Attenuation And Cross Polarization Measurements at 11.7 GHz.* Final Report prepared for NASA Goddard Space Flight Center (under Contract NAS 5-22576), The University of Texas, May 1979.

23. Neessen, J.; and Reinders, M.: "The Experimental Earth Station of the Netherlands PTT and Results of Propagation Measurements With the SIRIO Satellite." *Alta Freq.*, vol. XLVIII, no. 6, June 1979, pp. 399-407.

24. Dosch, Christoph: "Propagation Measurements in Munich Using the 11.6 GHz Beacon of the SIRIO Satellite." *Alta Freq.*, vol. XLVIII, no. 6, June 1979, pp. 363-367.

25. Capsoni, C.; Mauri, M.; Paraboni, A.: "Cumulative Attenuation Statistics at 11.6 and 17.8 GHz." *Alta Freq.*, vol. XLVIII, no. 6, June 1979, pp. 377-383.

26. Otsu, Y.; Furuhama, Y.; Hoshina, S.; and Shiro, I.: "Propagation Measurements and TV-Reception Tests With the Japanese Broadcasting Satellite for Experimental Purposes." *IEEE Trans. Broadcast.*, vol. BC-25, no. 4, Dec. 1979, pp. 113-120.

27. Lin, S. H.; Bergman, H. J.; and Pursley, M. V.: "Rain Attenuation on Earth Satellite Paths—Summary of 10-Year Experiments and Studies." *Bell Syst. Tech. J.*, vol. 59, no. 2, Feb. 1980, pp. 183, 228.

28. Tang, D. D.: *19/29 GHz Propagation Experiment Annual Report.* TR 79-471.4, GTE Laboratories Inc. (Waltham, Mass.), Nov. 1979.

29. Goldhirsh, J.: "Cumulative Slant Path Rain Attenuation Statistics Associated With the Comstar Beacon at 28.56 GHz for Wallops Island, Va." *IEEE Trans. Antennas Propagat.*, vol. AP-27, no. 6, Nov. 1979.

30. "Radiometeorological Data." Rept. 563, International Radio Consultative Committee (CCIR) (Geneva), 1972.

31. "Radiometeorological Data." Rept. 563-1, Doc 5/1022-E, International Radio Consultative Committee (CCIR), XIVth Plenary Assembly (Kyoto), 1978.

32. Rice, P. L.; and Holmberg, N. R.: "Cumulative Time Statistics of Surface Point-Rainfall Rates." *IEEE Trans. Commun. Technol.*, vol. COM-21, no. 10, Oct. 1973.

33. Dutton, E. J.; and Dougherty, H. T.: *Modeling the Effects of Cloud and Rain Upon Satellite-to-Ground System Performance.* OT Rept. 73-5, Office of Telecommunications (Boulder, Colo.), Mar. 1973.

34. Dutton, E. J.: *Earth Space Attenuation Prediction Procedure at 4 to 16 GHz.* OT Rept. 77-123, Office of Telecommunications (Boulder, Colo.), May 1977.

35. Grantham, D. D.; and Kantor, A. J.: "Distribution of Radar Echoes over the United States." *Air Force Surveys in Geophysics,* Rept. 1191, AFCRL-67-0232, Mar. 1977.

36. Dutton, E. J.: "A Meteorological Model for Use in the Study of Rainfall Effects on Atmospheric Radio Telecommunications." Res. and Eng. Rept. OT/TREP-24, Office of Telecommunications, Dec. 1971.

37. Crane, R. K.: *Microwave Scattering Parameters for New England Rain.* Tech. Rept. 426, MIT Lincoln Laboratories, Oct. 1966.

38. Dutton, E. J.: *Earth Space Attenuation Predictions for Geostationary Satellite Links in the U.S.A.* NTIA Rept. 78-10, U.S. Dept. of Commerce (Boulder, Colo.), Oct. 1978.

39. Lin, S. H.: "Nationwide Long-Term Rain Rate Statistics and Empirical Calculation of 11 GHz Microwave Rain Attenuation." *Bell Syst. Tech. J.*, vol. 56, no. 9, Nov. 1977.

40. Lin, S. H.: "Empirical Rain Attenuation Model for Earth-Satellite Paths." *IEEE Trans. Commun. Tech.*, vol. COM-27, no. 5, May 1979.

41. Crane, R. K.: "A Global Model for Rain Attenuation Prediction." *EASCON '78 Record,* IEEE Pub. 78CH 1354-4 AES (Arlington, Va.), Sept. 1978, pp. 391-395.

42. Crane, R. K.: "Prediction of Attenuation ByRain." *IEEE Trans. Commun. Tech.*, to be published, 1980.

43. "Attenuation by Precipitation and Other Atmosphere Particles." CCIR Doc. 5/187-E, draft modifications to rept. 721, CCIR Study Groups Interim Meetings (Geneva), June 30, 1980.

44. Lin, S. H.: "Impact of Microwave Depolarization During Multipath Fading on Digital Radio Performance." *Bell Syst. Tech. J.*, vol. 56, no. 5, May 1977, pp. 645-674.

45. Shkarofsky, I. P.; and Nickerson, S. B.: "Multipath Depolarization Theory Combining Antenna With Atmospheric and Ground Reflection Effects." URSI Commission F Int. Symp. (Lennoxville, Canada), May 26-30, 1980.

46. Oguchi, T.: "Attenuation of Electromagnetic Wave Due to Rain With Distorted Raindrops." *J. Radio Res. Lab.*, vol. 7, no. 33, Sept. 1960. Part II, vol. 11, no. 53, Jan. 1964.

47. Chu, T. S.: "Rain-Induced Cross-Polarization at Centimeter and Millimeter Wavelengths." *Bell Syst. Tech. J.*, vol. 53, no. 8, Oct. 1974, pp. 1557-1579.

48. Arnold, H. W.; Cox, D. C.; Hoffman, H. H.; and Leck, R. P.: "Characteristics of Rain and Ice Depolarization for a 19- and 28-GHz Propagation Path From a Comstar Satellite." *IEEE Trans. Antennas Propagat.*, vol. AP-28, no. 1, Jan. 1980, pp. 22-28.

49. Pruppacher, H. R.; and Pitter, R. L.: "A Semi-Empirical Determination of the Shape of Cloud and Rain Drops." *J. Atmos. Sci.*, vol. 28, Jan. 1971, pp. 86-94.

50. Nowland, W. L.; Olsen, R. L.; and Shkarofsky, I. P.: "Theoretical Relationship Between Rain Depolarization and Attenuation." *Electron. Lett.*, vol. 13, no. 22, Oct. 27, 1977, pp. 676-678.

51. "Cross Polarization Due to the Atmosphere." CCIR Doc. 5/174-E, draft modifications to rept. 722, CCIR Study Groups Interim Meetings (Geneva), June 30, 1980.

52. Bostian, C. W.: *A Depolarization and Attenuation Experiment Using the COMSTAR and CTS Satellites, Final Report on Fourth Year of Work.* Virginia Polytechnic Institute and State University report (for NASA Contract NAS5-22577), Mar. 25, 1980.

53. Kennedy, D. J.: "Rain Depolarization Measurements at 4 GHz." *COMSAT Tech. Rev.*, vol. 9, no. 2B, Fall 1979, pp. 629-668.

54. Vogel, W. J.: *CTS Attenuation and Cross Polarization Measurements at 11.7 GHz.* Rept. No. 22576-1, University of Texas at Austin, June 1980.

55. Bostian, C. W.; and Allnutt, J. E.: "Ice Crystal Depolarization on Satellite-Earth Microwave Radio Paths." *Proc. IEEE*, vol. 126, no. 10, Oct. 1979, pp. 951-960.

56. "Radio Emission Associated With Absorption By Atmospheric Gases and Precipitation." *Recommendations and Reports to the CCIR*, 1978, vol. 5, Rept. 720, International Telecommunications Union (Geneva), 1978, pp. 103-106.

57. "Propagation Data Required for Space Telecommunications Systems." CCIR Doc. 5/183-E, proposed modifications to rept. 564-1, CCIR Study Groups Interim Meetings (Geneva), July 1, 1980.

58. Devasirvathm, D. M. J.; and Hodge, D. B.: *Amplitude Scintillations of Earth-Space Propagation Paths at 2 and 30 GHz.* Tech. Rept. 4299-4, Ohio State Univ. (under Contract NAS5-22575), Mar. 1977.

59. Theobold, D. M.; and Hodge, D. B.: "Gain Degradation and Amplitude Scintillation Due to Tropospheric Turbulence." Tech. Rept. 78229-6, Revision 1, Ohio State Univ., May 1978.

60. Oguchi, T., "Statistical Fluctuation of Amplitude and Phase of Radio Signals Passing Through the Rain." *J. Radio Res. Lab.* (Japan), vol. 9, no. 41, Jan. 1962.

61. Crane, R. K.: "Coherent Pulse Transmission Through Rain." *IEEE Trans. Antennas Propagat.*, vol. AP-15, no. 2, Mar. 1967.

62. Ippolito, L. J.: "ATS-6 Millimeter Wave Propagation and Communications Experiments at 20 and 30 GHz." *IEEE Trans. Aerosp. Electron. Syst.*, vol. AES-11, no. 6, Nov. 1975.

63. Cox, D.; Arnold, H. W.; and Leck, R. P.: "Phase and Amplitude Dispersion for Earth-Satellite Propagation in the 20 to 30 GHz Frequency Range." *IEEE Trans. Antennas and Propagat.*, vol. AP-28, no. 3, May 1980.

1. Report No.	2. Government Accession No.	3. Recipient's Catalog No.
NASA TP-1770		

4. Title and Subtitle	5. Report Date
RADIO-WAVE PROPAGATION FOR SPACE COMMUNICATIONS SYSTEMS	February 1981
	6. Performing Organization Code: EC-4

7. Author(s)	8. Performing Organization Report No.
Dr. Louis J. Ippolito	
	10. Work Unit No.

9. Performing Organization Name and Address	11. Contract or Grant No.
NASA Office of Space and Terrestrial Applications Communications and Information Systems Division Washington, D.C. 20546	

12. Sponsoring Agency Name and Address	13. Type of Report and Period Covered
National Aeronautics and Space Administration Washington, D.C. 20546	Technical Paper
	14. Sponsoring Agency Code

15. Supplementary Notes

Report manuscript was submitted as an invited paper to the proceedings of the Institute of Electrical and Electronics Engineers (IEEE).

16. Abstract

The most recent information on the effects of Earth's atmosphere on space communications systems has been reviewed. The design and reliable operation of satellite systems that provide the many applications in space which rely on the transmission of radio waves for communications and scientific purposes are dependent on the propagation characteristics of the transmission path. The presence of atmospheric gases, clouds, fog, precipitation, and turbulence causes uncontrolled variations in the signal characteristics. These variations can result in a reduction of the quality and reliability of the transmitted information. Models and other techniques are used in the prediction of atmospheric effects as influenced by frequency, geography, elevation angle, and type of transmission. Recent data on performance characteristics obtained from direct measurements on satellite links operating to above 30 GHz have been reviewed. Particular emphasis has been placed on the effects of precipitation on the Earth/space path, including rain attenuation, and rain and ice-particle depolarization. Other factors are sky noise, antenna gain degradation, scintillations, and bandwidth coherence. Each of the various propagation factors has an effect on design criteria for communications systems. These criteria include link reliability, power margins, noise contributions, modulation and polarization factors, channel cross-talk, error rate, and bandwidth limitations.

17. Key Words (Suggested by Author(s))	18. Distribution Statement
Depolarization Earth/space communications Propagation Rain attenuation	Unclassified—unlimited Subject Category 17

19. Security Classif. (of this report)	20. Security Classif. (of this page)	21. No. of Pages	22. Price
Unclassified	Unclassified	58	A04

For sale by the National Technical Information Service, Springfield, Virginia 22161

NASA-Langley, 1981

National Aeronautics and
Space Administration

Washington, D.C.
20546

Official Business
Penalty for Private Use, $300

THIRD-CLASS BULK RATE

Postage and Fees Paid
National Aeronautics and
Space Administration
NASA-451

NASA

POSTMASTER: If Undeliverable (Section 158 Postal Manual) Do Not Return